

# Targeted antisense oligonucleotide treatment rescues developmental alterations in spinal muscular atrophy organoids

---

Received: 15 May 2023

---

Accepted: 8 December 2025

---

Published online: 21 December 2025

---

 Check for updates

---

Irene Faravelli <sup>1,15,18</sup>, Paola Rinchetti <sup>1,16,18</sup>, Monica Tambalo <sup>2,18</sup>, Illia Simutin <sup>2</sup>, Lisa Mapelli <sup>3</sup>, Sara Mancinelli <sup>2,4</sup>, Matteo Miotto <sup>4</sup>, Mafalda Rizzuti <sup>5</sup>, Andrea D'Angelo<sup>1</sup>, Chiara Cordiglieri <sup>6</sup>, Giulia Forotti<sup>5</sup>, Clelia Peano<sup>7,17</sup>, Paolo Kunderfranco <sup>8</sup>, Luca Calandriello<sup>5</sup>, Giacomo P. Comi <sup>1,5</sup>, Elvezia Paraboschi<sup>2,4</sup>, Eleonora Pali<sup>3</sup>, Francesca Beatrice <sup>1</sup>, Egidio D'Angelo <sup>3,9</sup>, Serge Przedborski <sup>10,11,12,13</sup>, Monica Nizzardo <sup>5</sup>, Simona Lodato <sup>2,4</sup> ✉ & Stefania Corti <sup>1,14</sup> ✉

Spinal muscular atrophy (SMA) is a severe neurological disease caused by mutations in the *SMN1* gene, characterized by early onset and degeneration of lower motor neurons. Understanding early neurodevelopmental defects in SMA is crucial for optimizing therapeutic interventions. Using spinal cord and cerebral organoids generated from multiple SMA type 1 male donors, we revealed widespread disease mechanisms beyond motor neuron degeneration. Single-cell transcriptomics uncovered pervasive alterations across neural populations, from progenitors to neurons, demonstrating SMN-dependent dysregulation of neuronal differentiation programs. Multi-electrode array (MEA) analysis identified consistent hyperexcitability in both spinal and brain organoids, establishing altered electrical properties as a central nervous system-wide feature of pathogenesis. Early administration of an optimized antisense oligonucleotide (ASO) that increased SMN levels rescued morphological and functional deficits in spinal cord organoids across different genetic backgrounds. Importantly, this early intervention precisely corrected aberrant splicing in here identified *SMN1* targets enriched at critical nodes of neuronal differentiation. Our findings demonstrate that early developmental defects are core features of SMA pathogenesis that can be prevented by timely therapeutic intervention, providing insights for optimizing treatment strategies.

Spinal muscular atrophy (SMA) is a severe inherited neurological disorder and still one of the leading genetic causes of death in childhood<sup>1,2</sup>. SMA is caused by autosomal recessive mutations in *SMN1*, resulting in reduced expression of full-length SMN protein<sup>3</sup>. This leads to progressive degeneration of more vulnerable spinal motor neurons (MNs), causing proximal muscle weakness and atrophy, and early life-threatening respiratory failure<sup>4,5</sup>. SMA phenotypic spectrum is very

broad and consists of different clinical forms, from fatal to mild, which are ranked on the base of the motor milestones reached by the patients<sup>6</sup>.

The SMN protein is expressed in several fetal tissues, including the brain, spinal cord, skeletal muscle, heart, and kidney; it significantly decreases after birth, suggesting that SMN is particularly important during prenatal life<sup>7,8</sup>. Recent data from human SMA autopsies

associated abnormal MN axon development in utero with postnatal degeneration in SMA<sup>9</sup>. Beyond spinal cord involvement, defects in cognitive function and brain neuropathology have been reported in SMA patients, but only partially documented<sup>10</sup>. The early events that drive the degeneration as well as their impact on the entire central nervous system (CNS), are still largely unknown: considering pre-symptomatic factors is key when modeling the disease.

Recently, FDA/EMA approved breakthrough therapeutic strategies to restore the levels of SMN and they are currently in clinical use<sup>5,11</sup>. These approaches are based on either cDNA replacement of *SMN1* or the use of antisense oligonucleotides (ASOs) or small molecules to achieve splicing correction of *SMN2*. *SMN2* is a paralog of *SMN1* that produces a truncated and rapidly degraded SMN protein, which can be used as a point of action to restore SMN levels<sup>12</sup>. These drugs have dramatically changed the clinical prognosis of SMA, and for the fatal to severe SMA type I, are able to reduce the disease to a chronic condition by halting or preventing motor disability. Although growing clinical data show that approved treatments also provide benefits in the chronic phase, it is emerging that the greatest impact is achieved when patients are treated pre-symptomatically<sup>5</sup>. Remaining unmet therapeutic needs are the treatment of patients after symptom onset<sup>5</sup> and the elusive understanding of the factors halting treatment efficacy. Critically, even newborns identified through screening show incomplete motor recovery, particularly those with two *SMN2* copies<sup>13</sup>. Therefore, a better understanding of SMA mechanisms in prenatal disease stages is pivotal to optimizing current therapeutic approaches with the aim of increasing efficiency, targeting biodistribution, and developing new clinical strategies.

Conventional 2D cultures and animal models can only partially recapitulate the phenotypic and genetic complexity of human MN diseases. CNS 3D human organoids<sup>14–16</sup>, in contrast, display a high degree of cellular diversity, enabling them to model complex cell–cell interactions, while modeling the patient-specific genetic background.

Here, we leveraged an efficient protocol for the generation of induced pluripotent stem cell (iPSC)-derived spinal cord organoids (SCOs) and unveiled early clinically relevant SMA pathological phenotypes. We detected alterations in progenitors' behaviour, early neuronal differentiation defects, even before hallmarks of cell death appeared, and identified disease susceptibility for distinct neuronal subtypes, beyond MNs.

A pervasive alteration of the splicing machinery has been involved in several neurodegenerative diseases, and it has been recently postulated for the adult MN disease amyotrophic lateral sclerosis (ALS)<sup>17</sup>. SMN protein has a recognized role in the splicing machinery, but the impact of its disruption on developmental processes remains still unexplored. Using SCOs, we identified genes with abnormal splicing in SMA and those rescued by SMN-targeting therapies. This allowed us to study how restoring SMN reshapes the transcriptional landscape in patient-derived SCOs. Interestingly, we found that SMN deficiency disrupts the splicing of key genes involved in neural differentiation, potentially triggering SMA pathogenesis. Our findings demonstrate SMN critical role in neural development and the significance of its restoration in therapeutic strategies.

## Results

### SMN deficiency impacts progenitors and neurons in the spinal cord

We derived human SCOs from healthy control (CTRL,  $n = 5$ ) and SMA type I ( $n = 5$ ) patient-derived iPSCs lines (Supplementary Fig. 1 and Supplementary Data 1). Spinal cord development is a complex process that entails both rostral-caudal specification, mediated by Wnt and retinoic acid (RA), and dorso-ventral patterning, downstream of sonic hedgehog (SHH) signaling<sup>18,19</sup>. Thus, SCOs were cultured in the presence of small molecules acting on these pathways to recapitulate in vitro the spinal cord specification<sup>20–22</sup> (Fig. 1a). In both CTRL and

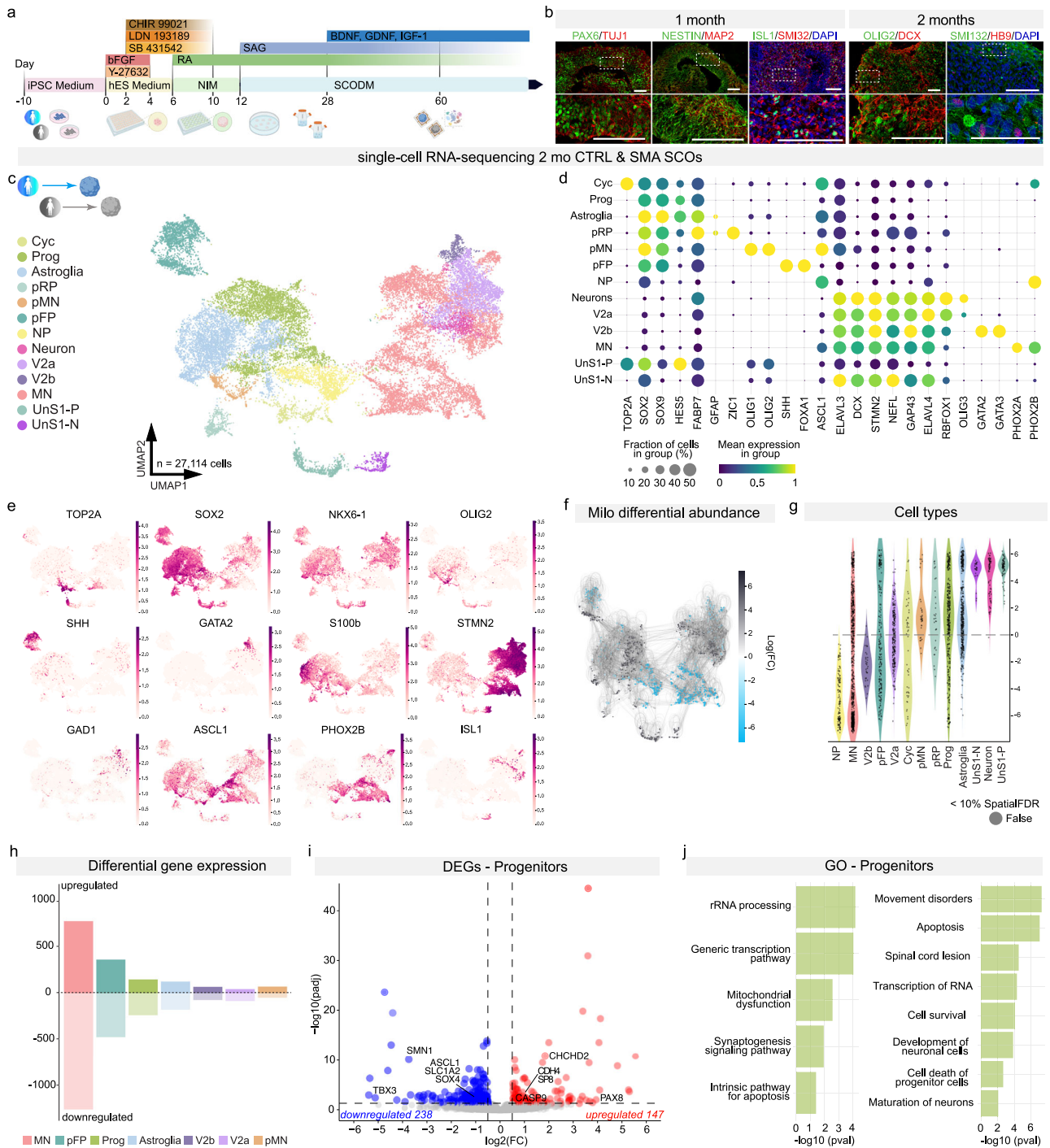
SMA organoids, the treatment promoted progressive caudal neuralization, as evidenced by the appearance of neuronal progenitors at the early differentiation stage (1 month), marked by the expression of PAX6 and NESTIN (Fig. 1b). This was followed by the appearance of the neuronal markers DCX and MAP2, indicating ongoing neuronal differentiation (Fig. 1b, Supplementary Fig. 2, and Supplementary Data 2 and 3). As the differentiation proceeded, we observed the presence of spinal precursors expressing HOXB4 and OLIG2 along with ISL1- and MNX1- positive MNs (Fig. 1b and Supplementary Fig. 2). At 2 months, we also detected the presence of astroglial cells (Supplementary Fig. 2). Together, the data show that SCOs can recapitulate key aspects of spinal cord neurogenesis.

To explore the early events driving SMA pathogenesis, we analyzed 2-month-old CTRL and SMA SCOs composition by single-cell RNA-seq (C1, C3, S1, and S3 lines, Fig. 1c–e, Supplementary Fig. 3, and Supplementary Data 4). Accounting for technical variability, we sequenced individual SCOs deriving from 2 CTRL and 2 SMA lines (Supplementary Data 1) and successfully profiled a total of 27,114 cells. Module annotation with defined sets of marker genes for dorsal and ventral domains identified different classes of neural progenitors (Prog, *SOX2*, *SOX9*), including floor plate progenitors (pFP, *SHH*), differentiating neurons (Neuron, *DCX*), and subtypes of spinal cord neuronal domains (Fig. 1c–e and Supplementary Fig. 3). At this stage, we could also identify distinct clusters of MN precursors (pMN, *OLIG2*) and postmitotic MNs (MN, *PHOX2B*, *ISL1*) (Fig. 1c–e, Supplementary Figs. 3d–g and 4, and Supplementary Data 4). The selective expression of defined combinations of HOX transcripts associated with a posterior neural tube patterning suggested the acquisition of a cervical spinal cord identity (Supplementary Fig. 3d). To benchmark CTRL SCOs against human embryonic and fetal spinal cord development, we used two complementary transcriptomic datasets. The first, a single-cell RNA-seq dataset spanning a broad range of developmental stages<sup>23</sup>, allowed us to identify the time point most closely resembling our organoids, revealing a strong transcriptional similarity with first-trimester spinal cord, peaking at gestational week 8 (Supplementary Fig. 3e). The second dataset<sup>24</sup>, a high-resolution single-cell atlas of the human fetal spinal cord (4–8 gestational weeks), enabled precise mapping of the cellular composition of SCOs. This analysis showed that SCOs closely matched major neural cell classes, including progenitors and neurons, while lacking similarity with mesodermal or endodermal lineages (Supplementary Fig. 3f, g). Together, these findings support the use of SCOs as a robust in vitro model for studying neurological diseases with multicellular involvement, such as SMA.

To investigate whether cell composition and relative contribution of neuronal types are altered in the absence of SMN protein, we performed a differential abundance test using the MiloPy framework<sup>25</sup> (Fig. 1f, g). This revealed that specific cell subtypes were differentially represented in SMA organoids, with MNs significantly decreased in SMA genotype.

We further extended our analyses to include pairwise comparisons between individual genotypes/lines in order to evaluate the consistency of our findings across conditions. Except for the C1 vs. S3 comparison, all line-to-line comparisons revealed a significant reduction in MN numbers in SMA relative to CTRL. Considering the inherent variability of the in vitro system, these results nevertheless demonstrate a significant reduction in MN numbers at this stage (Supplementary Fig. 5). Interestingly, in contrast with the reduction of MNs, pMNs were enriched in SMA organoids, as well as other clusters of neural progenitors (Fig. 1f, g). These results support a broader effect on neural diversity in the reduction of SMN, which impacts the proportion of different cell types in the developing organoids.

We therefore investigated the transcriptional changes associated with the lack of SMN in each cluster. To account for the differences in abundance presented in SMA SCOs, we performed differential gene



expression analysis in clusters presenting at least 25% of cells of each genotype (Fig. 1h and Supplementary Fig. 6; absolute log fold change  $\geq 0.5$  and adjusted  $p$ -value  $< 0.05$ ). While the largest proportion of deregulated genes (2031 genes differentially expressed between CTRL and SMA SCOs, 772 upregulated and 1259 downregulated) was observed in cells ascribed to the MN cluster, progenitor cells were the next most affected (Supplementary Data 5). Interestingly, specific genes related to progenitor fitness were downregulated (*ASCL1*, *SOX4*), while *CASP9*, involved in the apoptosis signaling, was upregulated (Fig. 1i). Gene ontology analysis on progenitors (Fig. 1j) revealed a pervasive effect of the lack of SMN on pathways involved in several developmental processes. Overall, these findings highlight the profound impact of SMN deficiency on the cellular composition and transcriptional landscape of SCOs. While the significant reduction in

spinal MNs is a key hallmark of SMA, the altered abundance and transcriptional dysregulation of progenitor cells reveal an equally critical aspect of the disease pathology with a broader disruption in neural development, often disregarded in the investigation of this disease.

**SMA progenitor defects precede motor neuron impairment**  
 To longitudinally capture the differentiation progression phenotype at the cellular level, we performed high-content image analysis (Fig. 2a–d). Notably, aberrant differentiation trajectories were observed in SMA SCOs. While CTRL SCOs showed a clear reduction in SOX2-expressing neural progenitors and an increase in the post-mitotic neuronal marker TUJ1 from 1 to 2 months, SMA SCOs exhibited a less pronounced reduction in SOX2 and no increase in the proportion

**Fig. 1 | CTRL and SMA SCOs display different subtypes of spinal cord cell populations.** **a** Schematics of human SCO generation. Created in BioRender. Rinchetti, P. (2025) <https://BioRender.com/l7ay5hq>. **b** Immunostaining of developmental and neuronal markers in SCOs at 1 and 2 months. SCOs exhibit positive staining for neurodevelopmental markers, including PAX6, NESTIN, and OLIG2 (green), as well as neuronal markers such as ISL1 (green), TUJ1, MAP2, SMI32, and DCX (red). Additionally, motor neurons are indicated by the positive expression of HB9 (red). Nuclei were stained with DAPI (blue). Scale bar: 100  $\mu$ m. Representative images. Immunostaining was performed independently on at least three different organoids per batch for a minimum of three CTRL and three SMA lines. **c** CTRL and SMA single cell RNA-sequencing at 2 months (mo) from the C1, C3, S1, and S3 lines. Unsupervised UMAP subdivides SCOs into neural progenitors (cycling cells (Cyc), progenitors (Prog), astroglia, progenitors roof plate (pRP), motor neuron progenitors (pMN), floor plate progenitors (pFP), neurogenic progenitors (NP)), differentiating neuronal cells (Neuron), several subtypes of ventral neurons (V2a, V2b), and motor neurons (MN), and a distinct cluster of unmatched SMA cells, specifically originating from the SMA S1 line (unmatched-S1 progenitors (UnS1-P), unmatched-S1 neurons (UnS1-N)). **d** Dot plots showing cluster-specific expression of

representative genes associated with cell differentiation; dot size corresponds to the percentage of cells in a cluster expressing each gene and the color corresponds to the average expression level (from violet to yellow, low to high). **e** UMAP feature plots showing the log-normalized counts of selected representative genes for proliferative factors (*TOP2A* and *SOX2*), progenitor markers (*NKX6-1*, *OLIG2*, *SHH*, *GATA2*) and neuronal differentiation markers (*STMN2*, *GADI*, *PHOX2B*, and *ISL1*). **f** Abstracted graph of neighborhoods of the results from Milo differential abundance testing. SMA enrichment in grey and CTRL enrichment in blue. **g** Violin plot showing the distribution of log-fold changes of differentially abundant neighborhoods assigned to cell type labels. **h** Numbers of deregulated genes across different clusters. **i** Volcano plot of differential gene expression (DEG) in progenitor clusters in SMA SCOs relative to CTRL. Values of log<sub>2</sub> Fold Change are plotted against  $-\log_{10}$  of the *q*-value for each gene. Red denotes genes upregulated in SMA, while blue denotes genes downregulated in SMA (absolute log fold change  $\geq 0.2$  min.pct = 0.25 and adjusted *q*-value  $< 0.05$ , thresholds plotted as dashed lines). **j** Selected Gene Ontology (GO) for upregulated and downregulated genes in the progenitor cluster performed with QIAGEN Ingenuity Pathway Analysis (IPA) software (Fisher test with Benjamini–Hochberg correction).

of TUJ1-expressing cells (Fig. 2a–d; percentage of SOX2-positive cells in each organoid at 1 vs. 2 months: CTRL 47.57%  $\pm$  11.94 vs. 20.40%  $\pm$  13.85,  $p < 0.0001$ ; SMA 38.79%  $\pm$  14.42 vs. 25.44%  $\pm$  13.91,  $p = 0.0148$ ; percentage of TUJ1 positive cells in each organoid at 1 vs. 2 months: CTRL 13.52%  $\pm$  4.788 vs. 28.42%  $\pm$  12.35,  $p = 0.0002$ ; SMA 21.49%  $\pm$  14.28 vs. 13.84%  $\pm$  6.759,  $p = 0.0764$ ). Accordingly, the SOX2/TUJ1 ratio was significantly higher in the control group at day 30 ( $p = 0.0444$ ) but showed a marked decrease by day 60, indicating a shift from progenitor cells to differentiated neurons over time, in line with the expected physiological trajectory. However, this pattern was not observed in the SMA condition (Fig. 2e).

Since SCOs recapitulate the early stage of spinal cord development, and our data suggest that the physiological process of cell death could be enhanced in SMA, we longitudinally tested CTRL and SMA SCOs for programmed cell death. SMA SCOs indeed exhibited a difference in apoptosis dynamics in comparison with CTRL SCOs, with a steep enhancement at 2 months (percentage of apoptotic nuclei in each organoid at 1 vs. 2 months: CTRL 11.30%  $\pm$  2.512 vs. 7.369%  $\pm$  5.125,  $p = 0.3786$ ; SMA, 4.245%  $\pm$  2.372 vs. 23.02%  $\pm$  11.34,  $p < 0.0001$ ; Supplementary Fig. 7a, b). Enrichment analysis of apoptosis-related biological functions, based on differentially expressed genes (DEG) between SMA and CTRL SCOs, revealed that these processes were predominantly upregulated in SMA pMNs and MNs (Supplementary Fig. 7c).

Differences in cell death rate might explain, at least in part, the reduced MN population in SMA SCOs captured by MiloPy (Fig. 1f, g), while the altered cell type composition suggests changes in early developmental programs in SMA tissue.

To examine differences in developmental dynamics from progenitors to neuronal states, we performed pseudotemporal ordering of cells using CytoTRACE, implemented via the CellRank framework (Fig. 2e). This method infers cellular differentiation status based on transcriptional complexity, and importantly, it is agnostic to the choice of root cell, allowing unbiased pseudotemporal ordering without requiring prior assumptions about lineage starting points. In line with *in vivo* human fetal development<sup>24</sup>, CTRL organoids displayed a continuous progression from progenitor populations to differentiated neuronal cell types (Fig. 2e, f). In contrast, SMA SCOs displayed a significant global shift toward lower developmental maturity (Kolmogorov–Smirnov (KS) test,  $p = 2.16 \times 10^{-8}$ ) that could also be shown across all genotypes (Supplementary Fig. 9). Cell-type-specific analyses further revealed a robust, statistically significant divergence in the pseudotime score distributions (Fig. 2g).

Altogether, these data support our previous results pointing at an early alteration in SMA neurodevelopment, where cells pause at intermediate developmental states unable to proceed along their

maturation, which could, in turn, impact in their ability to survive in the nascent circuits.

### SMA motor neuron developmental trajectory is hindered

To investigate gene expression changes during MN differentiation, we partitioned the dataset to focus specifically on MN lineage, including pMNs, early and mature MNs (Fig. 3 and Supplementary Fig. 8). We identified the main categories of somatic MNs, with little to no evidence of a distinct visceral MN population, as visceral markers were either absent or co-expressed with skeletal MN markers (Supplementary Fig. 8b). Using diffusion mapping of the MN lineage subset, we visualized eight distinct transcriptional clusters (Supplementary Fig. 8a) corresponding to three individual MN subtypes based on the expression levels of *PHOX2B* vs. *ISL1/MNX1* (Supplementary Fig. 8b–e). Despite the overall higher abundance of MN cells in CTRL genotypes (Fig. 1f, g), the MN-1 *ISL1*<sup>+</sup>/*MNX1*<sup>+</sup> subpopulation was preferentially enriched in SMA genotypes.

Next, we explored developmental pathways within the MN partition, allowing us to map the neurogenic progression from pMN to mature MNs (Fig. 3a–c). In CTRL SCOs, the neurogenic trajectory from pMNs to MNs followed the expected sequential progression during differentiation (Fig. 3b, c). A different scenario emerged in the MN differentiation trajectory of SMA SCOs. In contrast to the continuous progression seen in CTRL samples, the differentiation trajectory in SMA appeared polarized. This polarization was characterized by a concentration of cells at the progenitor state at the beginning of the trajectory, an accumulation of cells in an intermediate state, and a notable enrichment of MNs at the end of the trajectory, predominantly within a single branch (Fig. 3c). Importantly, consistent results were obtained when the dataset was analyzed by individual cell lines, suggesting that while the relative abundance of MNs differs among lines, the underlying developmental alteration is a shared feature across all (Supplementary Fig. 9). This suggests that SMN deficiency may disrupt the progressive acquisition of fate along MN differentiation, leading to an imbalance between progenitors and terminally differentiated neurons.

The interplay between specific transcription factors (TFs) is pivotal for the execution of correct developmental programs in the spinal cord<sup>26</sup>; cell-type-specific TFs represent central hubs in gene regulatory networks and alteration of their expression is associated with downstream defects in cell identity acquisition and maintenance<sup>18</sup>. To investigate whether the early developmental defects associated with SMA disease were driven by changes in TF activity, we used pySCENIC (Single-Cell Regulatory Network Inference and Clustering) algorithm<sup>27</sup> as a tool for the selection of key TFs along the developmental trajectory of CTRL and SMA SCOs organoids

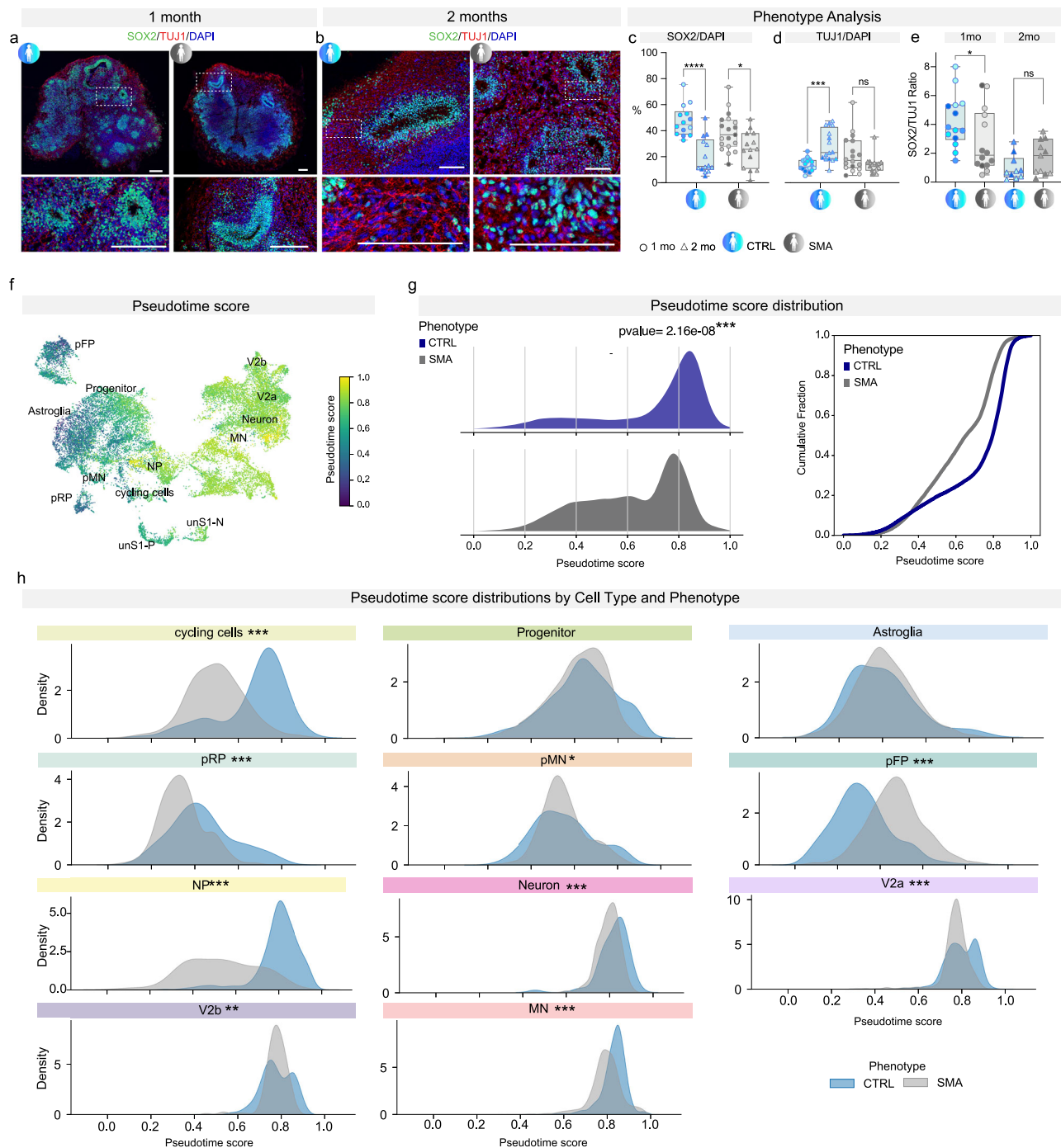


**Fig. 2 | Neurodevelopmental disease signatures of SMA SCOs.**

**a, b** Representative images of SOX2 (green) and TUJ1 (red) staining at 1 and 2 mo in CTRL and SMA SCOs. Scale bar: 200  $\mu$ m. Nuclei were stained with DAPI (blue). **c** Quantification of SOX2-positive cells (as a percentage of cells revealed by DAPI staining) at 1 (circles) and 2 mo (triangles) (two-way ANOVA, Sidak's multiple comparisons test:  $p < 0.0001$  and  $p = 0.0148$  for CTRL and SMA, respectively.  $n = 28$  from D30 and D60 CTRL SCOs;  $n = 4$  C1,  $n = 4$  C2,  $n = 3$  C4,  $n = 3$  C5;  $n = 8$  C1,  $n = 3$  C4,  $n = 3$  C5;  $n = 33$  from D30 and D60 SMA SCOs  $n = 4$  S1,  $n = 7$  S2,  $n = 6$  S4,  $n = 2$  S5;  $n = 5$  S2,  $n = 4$  S3,  $n = 5$  S4). **d** Box plots show the minimum and maximum value in the series along with median and 25–75 percentile. **e** Expression of TUJ1 increase over time in the CTRL, meanwhile in the SMA SCOs there is a trend of decreasing in the expression of TUJ1 (two-way ANOVA, Sidak's multiple comparisons test:  $p = 0.0002$  and  $p = 0.0764$  for CTRL and SMA, respectively.  $n = 33$  from D30 and D60 CTRL SCOs  $n = 4$  C1,  $n = 5$  C2,  $n = 3$  C3,  $n = 3$  C4,  $n = 3$  C5;  $n = 4$  C1,  $n = 3$  C2,  $n = 3$  C3,  $n = 3$  C4,  $n = 2$  C5;  $n = 33$  from D30 and D60 SMA SCOs  $n = 4$  S1,  $n = 2$  S2,  $n = 4$  S3,  $n = 6$  S4,

$n = 2$  S5;  $n = 4$  S1,  $n = 3$  S2,  $n = 3$  S3,  $n = 5$  S4). **e** Stacked bar plot showing the ratio of SOX2 and TUJ1 at 1 mo and 2 mo in CTRL and SMA SCOs. (Mann-Whitney test:  $p = 0.0444$  and  $p = 0.1734$  CTRL vs. SMA at 1 mo and 2 mo, respectively.  $n = 24$  from D30 and D60 CTRL SCOs  $n = 4$  C1,  $n = 4$  C2,  $n = 3$  C4,  $n = 3$  C5;  $n = 5$  C1,  $n = 3$  C4,  $n = 2$  C5;  $n = 25$  from 1 mo and 2 mo SMA SCOs  $n = 4$  S1,  $n = 2$  S2,  $n = 6$  S4,  $n = 2$  S5;  $n = 3$  S2,  $n = 3$  S3,  $n = 5$  S4). **f** UMAP plot showing cells colored by pseudotime score, with label annotation of major cell types. **g** Left: Density plots of pseudotime score distributions in CTRL (blue) and SMA (gray) cells (two-sided Kolmogorov–Smirnov (KS) test,  $p = 2.16 \times 10^{-8}$ ). Right: Cumulative distribution plot of pseudotime scores in CTRL and SMA cells. **h** Density plots of pseudotime scores for individual cell types, comparing CTRL (blue) and SMA (gray). Significant differences in pseudotime distributions were assessed using the two-sided KS test. Asterisks indicate significance levels (\* $p < 0.05$ , \*\* $p < 0.01$ , \*\*\* $p < 0.001$ , \*\*\*\* $p < 0.0001$ ). Source data are provided as a Source Data file.

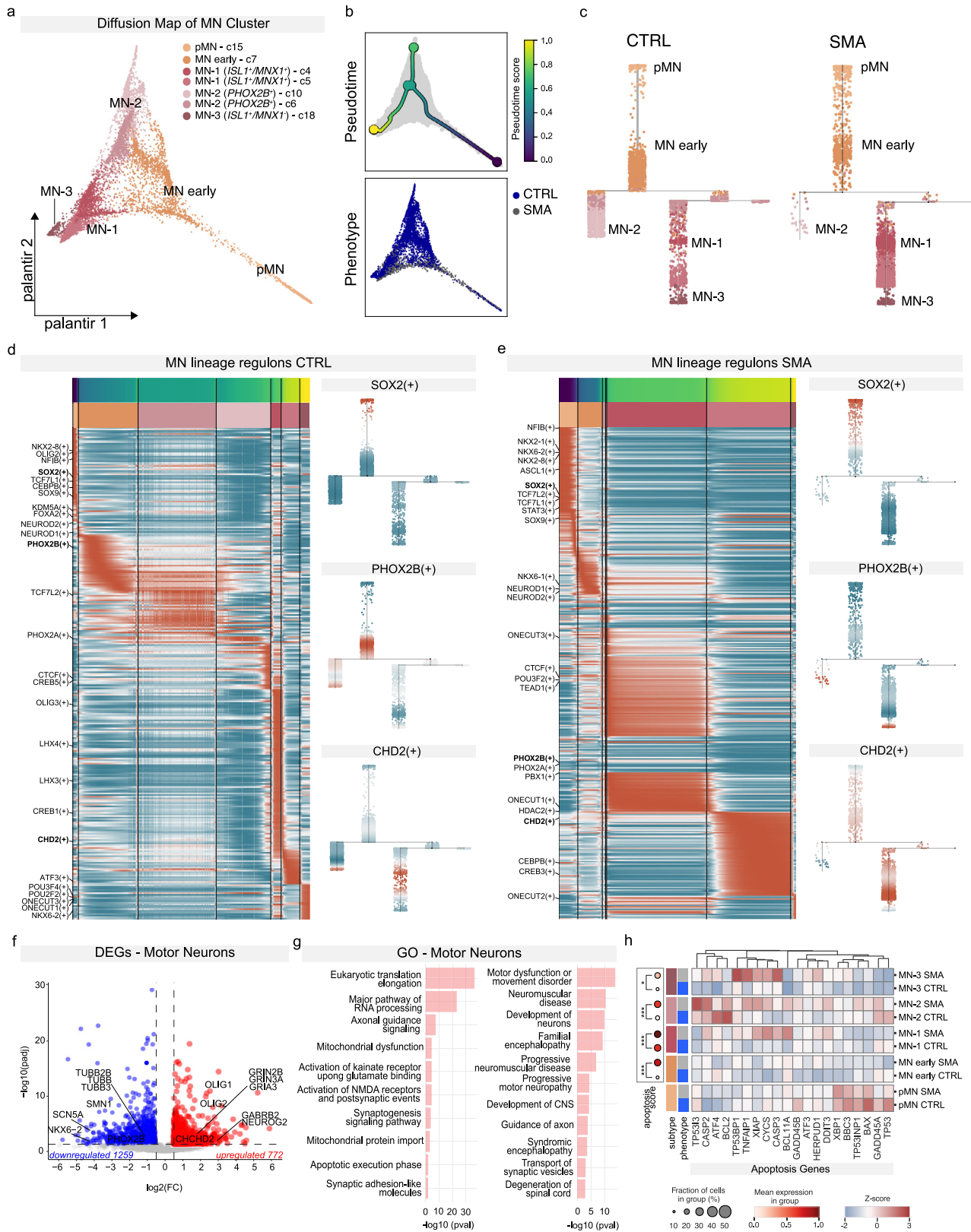


(Fig. 3d, e). Interestingly, we found several TFs known to control key aspects of the molecular development of the human spinal cord (i.e., *SOX2*, *SOX9*, *OLIG2*, *NKX6-1*) expressed along the different states of the trajectories in SMA and CTRL SCO (Fig. 3d, e), suggesting important variations in the activity of transcriptional programs among cell states in absence of SMN. Histone modifiers and regulators of chromatin architecture were also identified (*CHD2*, *HDAC2*, *KDM5A*), which could

be important determinants in human spinal cord development and could impact SMA disease course.

To determine whether the developmental TF expression implied differential gene regulatory programs, we calculated regulon activity. We observed that shared regulons of TFs key for MN differentiation (e.g., *SOX2*, *PHOX2B*, *CHD2*) had shifted profile of activity in SMA, with a sustained activity of *SOX2*- transcriptional programs, which is

**Fig. 3 | SMA SCOs show molecular signatures of disease.** **a** Diffusion map (DM) of MN clusters colored by subcluster identity. **b** Top: DM colored by pseudotime score. Bottom: DM colored by sample phenotype (CTRL, SMA). **c** Projection of MNs onto the pseudotime trajectory for CTRL and SMA samples. Cells are colored by subcluster identity to show distribution along the trajectory. **d, e** Heatmap displaying regulon activity trends and pseudotime associated with the CTRL (**d**) and SMA (**e**) trajectories, binned by each subcluster identity. Regulon activity scores of *SOX2*, *PHOX2B*, and *CHD2* in CTRL and SMA samples. High level of regulon's activity in red and low level in blue. **f** Volcano plot of differential gene expression (DEG) in

MN clusters in SMA SCOs relative to CTRL. Values of  $\log_2$  Fold Change are plotted against  $-\log_{10}$  of the  $q$ -value for each gene. Red denotes genes upregulated in SMA, while blue denotes genes downregulated in SMA (absolute log fold change  $\geq 0.2$  min.pct = 0.25 and adjusted  $q$ -value  $< 0.05$ , thresholds plotted as dashed lines). **g** Selected Gene Ontology (GO) for upregulated and downregulated genes in motor neurons performed with QIAGEN Ingenuity Pathway Analysis (IPA) software (Fisher test with Benjamini–Hochberg correction). **h** Left: Dot plot showing expression of apoptosis module scores. Right: Heatmap of apoptosis-related gene expression across MN subclusters and phenotypes.

associated with the prolonged maintenance of progenitor states (Fig. 3d, e). Together, these analyses support the idea that, not only SMA SCOs fail to properly differentiate into mature MNs, but also show that the neuronal developmental trajectory, with the associated transcriptional regulations, is strongly altered from the early progenitor state. This might impinge on MN survival as well as influence the overall spinal cord neuronal differentiation.

We then looked at the transcriptional landscape of SMA vs. CTRL MNs (Fig. 3f, g). SMA MNs showed downregulation of genes involved in neuronal growth and synaptic maturation (*TUBB3*, *TUBB*, *SCNSA*). Notably, a small subset of genes showed consistent deregulation in virtually all cell types in SMA SCOs (Supplementary Data 5). They included *CHCHD2*, a mitochondrial protein involved in oxidative phosphorylation and whose upregulation was previously shown in other neurodegenerative conditions to be serving a compensatory protective response against oxidative stress<sup>28,29</sup>. Interestingly, *CHCHD2* has been shown to be subjected to alternative splicing. We validated by qPCR that this gene reproducibly displayed the same trend of deregulation across individual SCOs derived from two independent lines of CTRL and SMA (Supplementary Fig. 10a), while no difference was observed in multiple lines of undifferentiated SMA iPSCs (Supplementary Fig. 10b). Overall, SMA SCOs exhibit a disease-associated molecular signature across various MN maturation states, leading to global alterations in multiple molecular programs. Gene ontology analysis defined enriched categories related to metabolic processes, stress response and spinal cord disorders (Fig. 3g). Indeed, a significant reduction in neural projections (identified with staining for the heavy neurofilament NEF-H/SMI32, a marker gene enriched in MNs) was detected in SMA neurons derived from dissociated SCOs (CTRL  $59.17 \pm 12.30 \mu\text{m}$  vs. SMA  $34.62 \pm 8.34 \mu\text{m}$ ,  $p < 0.0001$ ; Supplementary Fig. 8f, g). Finally, we examined molecular programs associated with cell death by calculating module scores for apoptosis in each MN partition in CTRL vs. SMA conditions (Fig. 3h). We found a significant enrichment of cell death-related molecular programs in SMA MNs across all subgroups. This indicates that, although some MN subtypes are more represented in SMA at this time point, they not only exhibit dysregulation of developmental trajectories but have also already initiated degenerative cascades associated with MN loss.

### Pathological patterns of activity in SMA spinal cord organoids

Modifications in the electrophysiological activity of spinal MNs have previously been reported in 2D cultures<sup>30</sup> and pre-symptomatic mouse models of SMA<sup>31</sup>. As in other motor degenerative disorders<sup>32</sup>, this abnormal activity might contribute to the SMA human disease phenotype. However, it is not clear how early in disease progression this dysfunction occurs and how it varies across CNS compartments. We exploited high-density multi-electrode array (HD-MEA) technology to investigate the functionality of SCOs derived from SMA patients (Fig. 4a–c). Basal recordings of 2-month-old CTRL and SMA SCOs showed spontaneous spiking activity, with significantly lower frequencies in SMA SCOs (CTRL  $1.956 \pm 0.5354 \text{ Hz}$  vs. SMA  $1.355 \pm 0.6807 \text{ Hz}$ ,  $p = 0.0127$ ; Fig. 4b, c). Moreover, SMA SCOs significantly increased their firing frequency more than CTRL SCOs after a glutamatergic stimulus, suggesting an early dysfunction with features of hyperexcitability (CTRL  $44.06\% \pm 20.03$  vs. SMA  $91.03\% \pm 28.42$ ,  $p < 0.0001$ ; Fig. 4b, c).

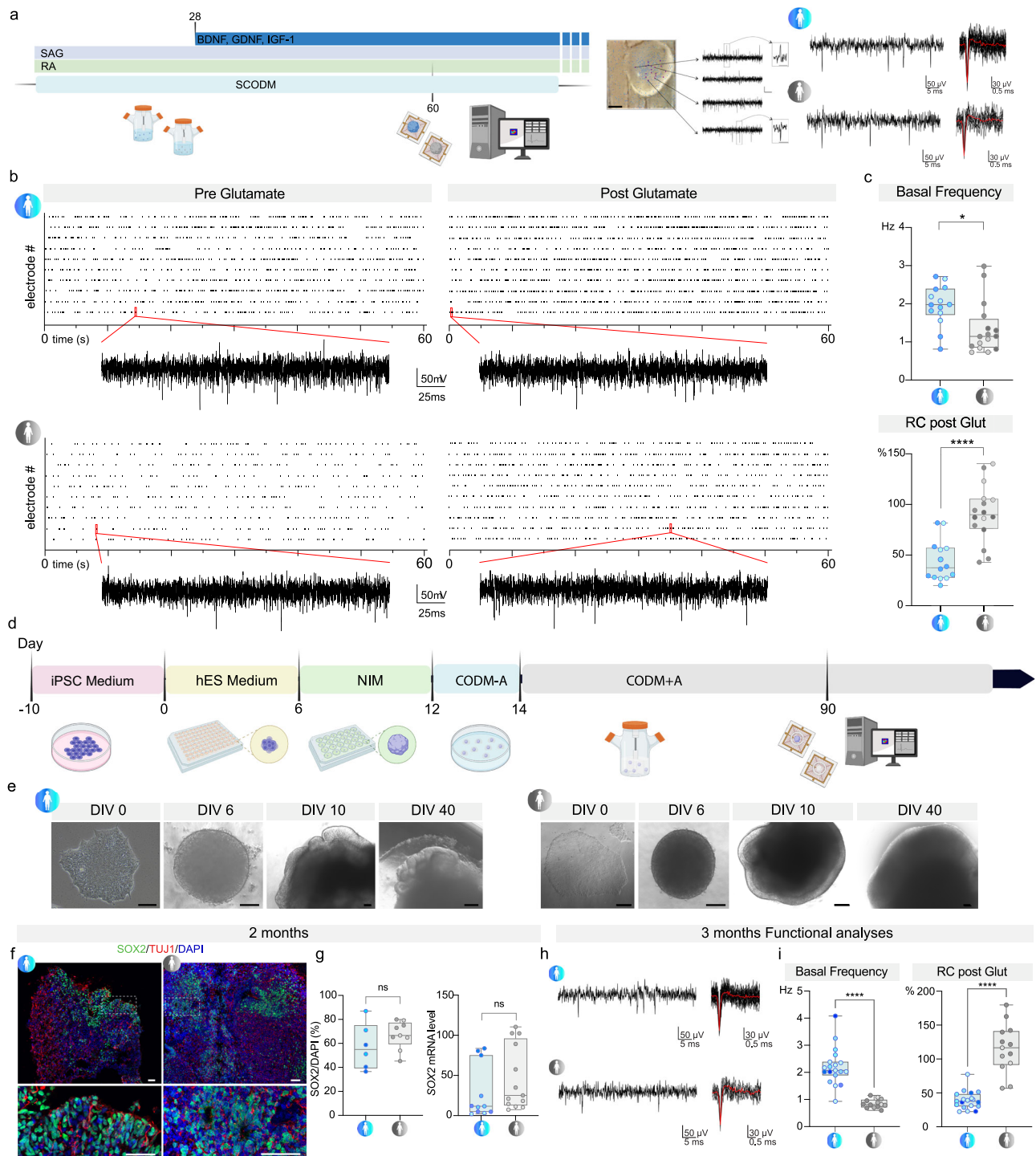
Notably, DEG analyses revealed, across different clusters, the presence of a set of deregulated genes related to synaptic channels among different neuronal populations, suggesting an overall impact on synaptic function (Supplementary Fig. 11a). To rule out changes in GABAergic transmission, we tested spontaneous firing frequency upon application, at the basal level, of gabazine and strychnine<sup>33</sup> to block GABA-A and glycine receptors. As expected, an increased spontaneous firing frequency was observed in CTRL organoids (CTRL  $44.21\% \pm 5.626$ ) and a similar behaviour was detected in SMA SCOs (SMA  $43.75\% \pm 16.4$ ,  $p = 0.9521$ ; Supplementary Fig. 11b–d). This response suggested the presence of active mechanisms of neuronal inhibition in the organoid circuits (CTRL  $43.71\% \pm 36.38$  vs. SMA  $35.72\% \pm 19.11$ ,  $p = 0.5455$ ). GAD65 staining confirmed the presence of inhibitory interneurons in both CTRL and SMA SCOs (Supplementary Fig. 11b lower panel), as also highlighted by single-cell molecular data. These results support the hypothesis that the observed hyperexcitability response of SMA organoids to glutamate does not imply a reduced inhibitory transmission, and it is more likely to be ascribed to alterations in glutamatergic transmission maturation.

Overall, we showed that SCOs display basal firing activity with the potential to respond to an exogenous stimulus and they generate functional circuits. Furthermore, SMA SCOs possess distinct electrophysiological properties, including increased glutamate sensitivity, that can potentially lead to hyperexcitability, a common trait of many neurodegenerative disorders.

### Pathological patterns of activity in SMA cerebral organoids

SMA has traditionally been considered a lower MN disease; nonetheless, cerebral involvement has been reported in the most severe SMA cases<sup>10</sup>. It is still debatable whether this feature is directly linked to SMA pathogenesis, or it is indirectly associated with spinal degeneration retrogradely spreading to the brain. To begin exploring these alternatives, we employed an adapted protocol for generating 3D cerebral organoids<sup>14</sup> from SMA and healthy iPSC lines (Fig. 4d, e and Supplementary Fig. 12), where a putative secondary effect of spinal cord degeneration was excluded. Both CTRL and SMA cerebral organoids displayed complex morphology, with heterogeneous regions containing neural progenitors (SOX2+), mainly localized within neural rosettes, and neurons (TUJ1+; Fig. 4f). We quantified the number of SOX2-positive progenitors across CTRL and SMA brain organoids at both the RNA and protein levels and did not detect a significant difference at the 2-month time point (CTRL  $57.45 \pm 19.10$  vs. SMA  $67.02 \pm 11.54$ ,  $p = 0.2449$ ; Fig. 4g). In parallel, we did not detect any significant difference for the expression of NEF-H/SMI32 (Supplementary Fig. 12c). Staining for glial populations (GFAP+), cortical neurons (CTIP2+ and SATB2+) and general neuronal markers (DCX and MAP2) at 2 months revealed the presence of a variety of cell types (Supplementary Fig. 12a, b). As for SCOs, brain differentiation can take place from SMA reprogrammed pluripotent cells and cerebral organoids are able to recapitulate key early steps of brain development.

Interestingly, cerebral organoids displayed abnormal electrophysiological activity like that seen in SMA SCOs. HD-MEA analysis (Fig. 4h, i) revealed that SMA cerebral organoids had a significantly lower basal spike frequency compared to CTRLs ( $2.206 \pm 0.6826 \text{ Hz}$



CTRL vs.  $0.8497 \pm 0.1629$  Hz SMA,  $p < 0.0001$ ; Fig. 4i). Consistent with the SCOs response observed after glutamatergic stimulation, SMA cerebral organoids increased their firing frequency by a significantly higher factor than CTRL organoids ( $115.3\% \pm 36.20$  SMA vs.  $39.11\% \pm 13.21$  CTRL,  $p < 0.0001$ ; Fig. 4i). Moreover, the presence of an active inhibitory neuronal circuit exploiting GABA-A (and likely glycine) receptors was detected (Supplementary Fig. 12d, e). Our results thus show pathological features in SMA cerebral organoids, demonstrating direct involvement of the disease in the CNS, beyond the spinal cord, and revealing the need to consider additional targets in the clinical therapeutic setting to evaluate the efficacy and the long-term response to treatments.

### Optimized SMN-targeted approach effectively restores cellular and functional alterations

Among the approved therapies for SMA<sup>12</sup>, nusinersen is based on an antisense oligonucleotide (ASO) acting on SMN2 (ASO\_10-27), increasing the overall levels of SMN protein. To determine if SMA SCOs are a suitable model for testing the effectiveness of potential therapies, and whether increasing SMN protein levels can correct specific molecular disease signatures, we tested a recently validated ASO for SMN2 with optimized morpholino chemistry (MO-10-34<sup>34,35</sup>) conjugated with an arginine-rich cell-penetrating peptide (r6-MO). We recently demonstrated that r6-MO can increase drug biodistribution and efficacy in animal models<sup>36</sup>.

**Fig. 4 | SMA SCOs and cerebral organoids (CrOs) show alterations to electrophysiological activity with features of hyperexcitability.** **a** Schematic of MEA analysis time-line and representative image of SCO on HD-MEA chip with recorded traces showing basal activity. Scale bar: 500  $\mu$ m. Elements of the schematic created in BioRender. Rinchetti, P. (2025) <https://BioRender.com/Oo9jsh1>. **b** Raster plot of CTRL and SMA SCOs pre- and post-glutamate. **c** Top: Quantification of basal firing activity in CTRL vs. SMA SCOs (unpaired *t*-test,  $p = 0.0124$ ,  $n = 29$  organoids from  $n = 5$  C1,  $n = 4$  C3,  $n = 5$  C4;  $n = 1$  S1,  $n = 4$  S2,  $n = 7$  S4,  $n = 4$  S5). Bottom: Relative change (RC) in firing frequency increase after glutamate (glut) perfusion in CTRL vs. SMA SCOs (unpaired *t*-test,  $p < 0.0001$ ,  $n = 30$  organoids from  $n = 5$  C1,  $n = 4$  C3,  $n = 5$  C4;  $n = 1$  S1,  $n = 4$  S2,  $n = 7$  S4,  $n = 4$  S5). Box plots show the minimum and maximum value in the series along with median and 25–75 percentile. **d** Schematic of human CrOs generation. Created in BioRender. Rinchetti, P. (2025) <https://BioRender.com/33yw3mr>. **e** Representative bright-field images of the progression of the differentiation pathway for CTRL and SMA CrOs. Scale bar = 100  $\mu$ m. **f** Representative images of SOX2 (green) and TUJ1 (red) staining at 2 mo in CTRL and SMA CrOs.

Scale bar: 200  $\mu$ m. Nuclei were stained with DAPI (blue). **g** Quantification of SOX2 as a percentage of positive nuclei and analysis of mRNA level in CrOs at 2 months. In both analysis the expression of SOX2 does not differ in CTRL and SMA CrOs (Left graph: unpaired *t*-test,  $p = 0.2449$ ;  $n = 15$  organoids from  $n = 3$  C3,  $n = 3$  C5;  $n = 5$  S1,  $n = 4$  S3. Right graph: unpaired *t*-test,  $p = 0.2524$ ;  $n = 24$  organoids from  $n = 2$  C1,  $n = 2$  C3,  $n = 1$  C4,  $n = 3$  C5,  $n = 3$  C6;  $n = 3$  S1,  $n = 3$  S2,  $n = 7$  S3). Box plots show the minimum and maximum value in the series along with median and 25–75 percentile. **h** Representative traces of basal recording of CTRL and SMA CrOs (3 mo). **i** Left: Basal firing frequency was lower in SMA CrOs than in CTRL (unpaired *t*-test,  $p < 0.0001$ ,  $n = 32$  organoids from  $n = 8$  C1,  $n = 3$  C2,  $n = 4$  C3,  $n = 4$  C6;  $n = 2$  S1,  $n = 5$  S3,  $n = 6$  S4). Right: the relative increase in firing frequency after glutamate (glut) perfusion was greater in SMA than in CTRL CrOs (unpaired *t*-test,  $p < 0.0001$ ,  $n = 32$  organoids from  $n = 8$  C1,  $n = 3$  C2,  $n = 4$  C3,  $n = 4$  C6;  $n = 2$  S1,  $n = 5$  S3,  $n = 6$  S4). Box plots show the minimum and maximum value in the series along with median and 25–75 percentile. Source data are provided as a Source Data file.

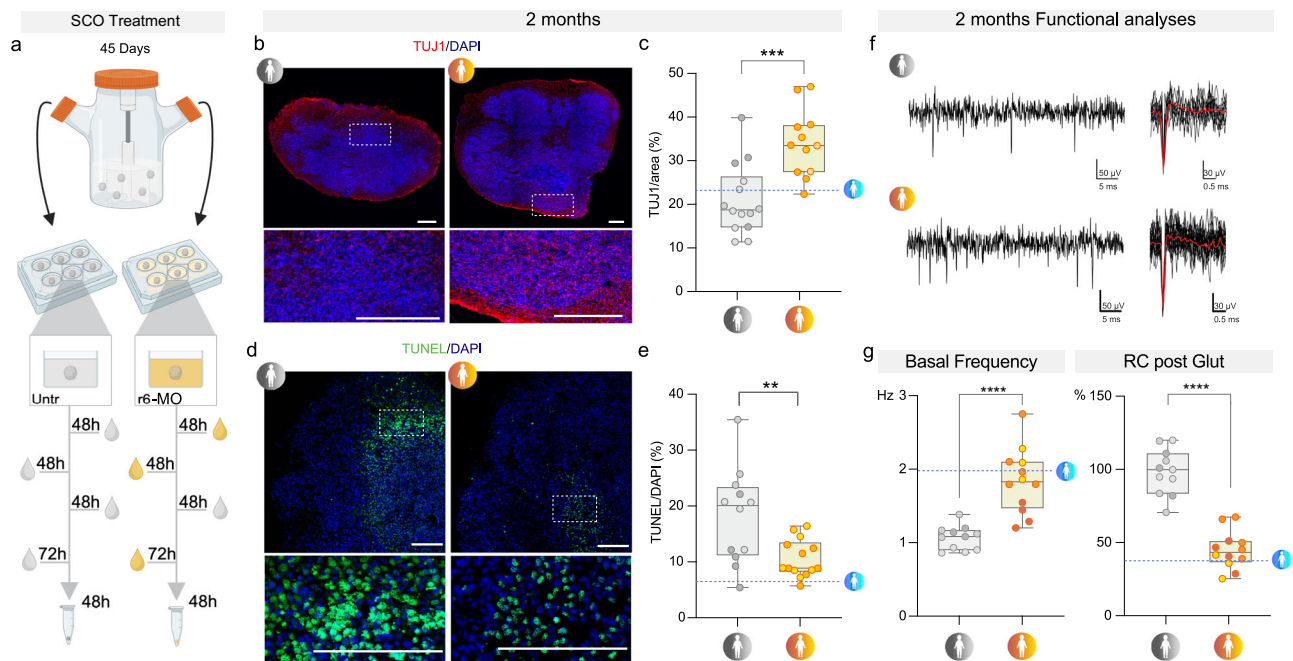


**Fig. 5 | SMA organoids display specific cellular features that are rescued by r6-morpholino.** **a** Schematic representation of r6-morpholino (r6-MO) treatment. SMA SCOs were treated three times for 48 h: T1, T2 48 h later, T3 72 h after the media was changed without the compound. Created in BioRender. Rinchetti, P. (2025) <https://BioRender.com/cd9gra2>. **b** Representative images of TUJ1 staining of Untr and r6-MO-treated SMA SCOs at 2 mo. Scale bar: 300  $\mu$ m. Nuclei were stained with DAPI (blue). **c** TUJ1 expression (intensity/area) is greater in r6-MO-treated SCOs than in untreated SCOs (unpaired *t*-test,  $p = 0.0003$ ,  $n = 26$  organoids from untreated  $n = 7$  S1,  $n = 3$  S2,  $n = 4$  S3, treated  $n = 7$  S1,  $n = 3$  S2,  $n = 2$  S3). Box plots show the minimum and maximum value in the series along with median and 25–75 percentile. **d** Representative images of TUNEL staining of Untr and r6-MO-treated SMA SCOs at 2 mo. Scale bar: 300  $\mu$ m. Nuclei were stained with DAPI (blue). **e** TUNEL-positive cells were less frequent in r6-MO-treated SCOs than in Untr SCOs

(unpaired *t*-test,  $p = 0.0050$ ,  $n = 26$  organoids from untreated  $n = 4$  S1,  $n = 3$  S2,  $n = 5$  S3, treated  $n = 4$  S1,  $n = 3$  S2,  $n = 7$  S3). Box plots show the minimum and maximum value in the series along with median and 25–75 percentile. **f** Representative traces of basal recording of Untr and r6-MO-treated SMA SCOs at 2 mo. **g** Left panel: Quantification of basal firing activity in Untr vs. r6-MO (unpaired *t*-test,  $p < 0.0001$ ,  $n = 23$  organoids from untreated  $n = 4$  S1,  $n = 4$  S2,  $n = 3$  S3, treated  $n = 4$  S1,  $n = 5$  S2,  $n = 3$  S3). Right panel: Relative change (RC) in the firing frequency decrease in r6-MO-treated SCOs compared to the Untr after glutamate perfusion (glut) (unpaired *t*-test,  $p < 0.0001$ ,  $n = 23$  organoids from untreated  $n = 4$  S1,  $n = 4$  S2,  $n = 3$  S3, treated  $n = 4$  S1,  $n = 5$  S2,  $n = 3$  S3). Box plots show the minimum and maximum value in the series along with median and 25–75 percentile. Source data are provided as a Source Data file.

First, we investigated whether unconjugated MO-10-34 and the r6-MO could increase SMN protein levels in SMA SCOs. SMA SCOs were treated at day 45 with either unconjugated (bare) MO or r6-MO (2.4 nmoles), or their respective custom-made scrambled sequences, for 48 h. This treatment was repeated three times with increasing doses (up to 4.8 nmoles) (Fig. 5a and Supplementary Fig. 13a). SMN reduction is a hallmark of SMA pathology (Supplementary Fig. 13b). We therefore first assessed whether our treatment could increase both SMN protein and mRNA levels. A significant increase in SMN protein expression was observed in lysates from r6-MO-treated organoids compared to untreated controls at later time points (Supplementary Fig. 13c).

Biotin-tagged r6-MO was detected both at the periphery and within the central core of the organoids (Supplementary Fig. 13d), indicating effective and widespread tissue distribution. Consistent with this, treatment with either r6-MO or MO-10-34 (bare morpholino) led to a significant upregulation of *SMN* mRNA levels compared to their respective scramble controls across all treated lines (S1, S2, and S3) (Supplementary Fig. 13e, f). To specifically examine the expression of *SMN1* and *SMN2* isoforms, we performed restriction fragment length polymorphism (RFLP) analysis in CTRL, untreated SMA, scramble-treated SMA, and r6-MO-treated SMA lines. This analysis confirmed that r6-MO treatment significantly reduced the levels of the truncated

*SMN2* Δ7 isoform in favor of the full-length transcript (Supplementary Fig. 13g).

Notably, the differentiation phenotype was completely restored by r6-MO treatment (percentage of cells positive for TUJ1: SMA 20.99% ± 8.044 vs. r6-MO 33.93% ± 7.648,  $p = 0.0003$ ; Fig. 5b, c). The administration of r6-MO at day 45 was also able to significantly prevent cell death (percentage of apoptotic nuclei in each organoid at 2 months: untreated 18.16% ± 8.443 vs. r6-MO 10.58% ± 3.37,  $p = 0.005$ ; Fig. 5d, e), supporting the idea that early intervention could halt the aberrant cellular processes, positively changing the course of the disease.

Strikingly, at the functional level, treatment with r6-MO resulted in enhanced basal activity compared to untreated SMA SCOs (r6-MO 1.843 ± 0.4396 Hz vs. untreated 1.067 ± 0.1623 Hz,  $p < 0.0001$ ; Fig. 5f, g), which was paralleled by a reduced response to the glutamatergic stimulus (percentage increase in frequency r6-MO 44.76% ± 12.81% vs. untreated 98.31% ± 15.56%,  $p < 0.0001$ ; Fig. 5f, g).

These findings reveal that fundamental cellular and functional phenotypes could be rescued by an early specific SMN-increasing therapy across multiple genetic backgrounds. Taken together, these data provide insights into the value of optimized ASOs and their impacts on the early treatment of SMA pathology.

### SMA splicing defects are rescued by SMN-increasing therapy

Disease-modifying therapies are currently changing the natural history of SMA, but the specific molecular pathways affected by SMN-targeted approaches and what is their impact on the different cell types along the developmental trajectory are not fully elucidated. We leveraged our platform to dissect the molecular drivers responsible for the rescue in the cellular and functional phenotypes. The SMN protein has a well-recognized crucial role in the splicing machinery<sup>37</sup>. Thus, by RNA deep-sequencing, we investigated changes in splicing events in SMA SCOs, and assess the splicing modifications induced by the MO treatment. We analyzed CTRL ( $n = 3$  lines, 3 individual replicates), SMA ( $n = 2$  lines, 4 individual replicates), and SMA-treated SCOs ( $n = 2$  lines, 4 individual replicates) after a two-month differentiation period, following treatment with r6-MO and r6-scrambled-MO as negative control (Supplementary Fig. 14).

In SMA vs. CTRL SCOs, an overall transcriptional alteration was confirmed with 666 genes were upregulated and 463 were downregulated (Supplementary Fig. 14a and Supplementary Data 6). GO analyses revealed enrichment for progressive encephalopathy disorder, while showing a downregulation for synaptogenesis and glutamate receptor signaling (Supplementary Fig. 14b). These findings correlate with the alterations in functional activity displayed by SMA SCOs. Since bulk-tissue RNA-sequencing reveals averaged gene expression patterns across entire organoids, we employed our single-cell expression data to infer gene modules and understand co-expression in specific cell types. This analysis identified 5 distinct modules with genes enriched in specific cell types: cycling cells (M1: *CDK1, CDKN3, NUSAP1, TOP2A, UBE2S*), progenitors (M2: *BTG1, EFNBL1, HES2/4, TUBA1C*), astroglia and progenitors (M3: *GABBR2, NTRK2, PHGDH, PTPRR1, SLC1A4*), intermediate progenitors/early MNs (M4: *FOXP4, RARA, SPI, TEAD2/3, TCF3*), and mature MNs (M5: *GRIA1/2/4, MAPT, NEFL, SCN2A*) (Supplementary Fig. 14c and Supplementary Data 6). These data further suggest a pervasive phenotype, involving distinct developmental dynamics, where MNs, along with differentiating cells, are significantly affected by the lack of *SMN1*.

To uncover the molecular mechanisms downstream of r6-MO treatment and elucidate the pathways leading to functional rescue, we compared the transcriptional and splicing landscapes of r6-MO-treated SMA SCOs with those treated with r6-scrambled-MO. The r6-scrambled-MO treatment served as a negative control, providing a baseline for comparison with r6-MO treatment. Relatively few transcriptional changes were detected after r6-MO treatment compared to

r6-scrambled-MO, suggesting that, at least within the considered time window, a global transcriptional change is not required for phenotypic rescue.

In contrast, analysis of pre-mRNA splicing patterns in SMA vs. CTRL, and r6-MO vs. r6-MO-scrambled treated SMA organoids showed substantial differences across conditions (Fig. 6a, b and Supplementary Fig. 14d). The loss of *SMN1* in SMA patients SCOs (comparing CTRL with SMA organoids) and SMN rescue by r6-MO treatment (comparing r6-scrambled-MO with r6-MO) led to multiple significant alternative splicing changes. The most altered events resulting were found as skipped exon (SE), mutually exclusive exons (MXE), followed by intron retention (IR), alternative 3' (A3SS) and 5' (A5SS) splice site events, detected with a lower frequency (Supplementary Data 7). To assess how r6-MO treatment affects the splicing landscape of SMA cells, we compared pre-mRNA splicing events in r6-MO-treated SCOs to those in r6-scrambled-MO (baseline control) treated cells. A total of 2,614 splicing events resulted to be specifically modified by r6-MO (Fig. 6c and Supplementary Data 8). The most abundant ones were represented by SE, MXE, and IR in similar proportions to the ones observed for the comparison of CTRL vs. SMA. We could identify 1982 genes specifically associated with the 2614 rescued splicing events (Supplementary Data 8). Gene ontology enrichment analysis of these genes showed significant enrichment for regulation of chromatin organization, DNA metabolic process, and cell cycle, as well as axon guidance and neurodegeneration (Fig. 6c). Importantly, changes in splicing events could be aligned with specific gene modules from the single cell RNA-seq analysis (Fig. 6d). We leveraged all the detected rescued spliced genes to compute module score analysis, revealing unique combinations of spliced genes specifically associated with cycling cells (M1: *BRIPI, CENPK, HMMR, TOP2A, UBE2C*), progenitors (M2: *ALG3, EIF5, LTN1, MRPL21, MRPL13*), progenitors and neurons (M3: *AH11, CEP290, KIAA0586, VPS13C, XPO1*) astroglia (M4: *BMPRI1, DDX3X, PDGFRB, SIRT2, SLIT2*) and MN cell types (M5: *GRIA2, MAP2, SCN1A, SCN3B, STMN4*) (Fig. 6d).

Our findings indicate lineage-specific splicing alterations downstream of r6-MO treatment (Supplementary Data 9). To assess whether these changes restore the splicing landscape of specific genes toward control levels, we compared splicing events related to the SMA phenotype vs. CTRL with those induced by r6-MO (carrying along the scramble-MO as specific control of the treatment). To do that, we intersected splicing events induced in SMA vs. CTRL and r6-MO vs. r6-scrambled-MO conditions. This integrated analysis revealed a distinct set of splicing events rescued upon r6-MO treatment (Fig. 6e and Supplementary Data 9). Notably, genes outside this category (which did not fully recover their splicing pattern by the r6-MO treatment) were linked to broader pathophysiological processes, further suggesting a systemic involvement beyond spinal cord diseases (Supplementary Data 10). Early r6-MO treatment restored splicing isoforms in 98 genes (Supplementary Data 9), which were identified as top candidates in our bioinformatics analysis. These genes likely play a crucial role in alleviating the phenotypic defects of SMA, with several chromatin remodeling enzymes, *ARIH2, ATG4A/B, CHD9*, and *HDAC6*, emerging as key players. Over time, these targets may help re-establish the molecular profile of both progenitors and neurons, thus contributing to the observed cellular and functional rescue.

Among the rescued genes, we highlighted *CHD9* (Chromodomain Helicase DNA-binding protein 9), a key regulator of the cell cycle in embryonic stem cells<sup>38</sup>, and *HDAC6* (Histone Deacetylase 6), which is critical for motor neuron development and function through its roles in axonal transport, autophagy promotion, and neuroprotection<sup>39,40</sup> (Fig. 6f, sashimi plots). These findings suggest that rescued splicing events impact diverse cellular and molecular processes crucial for progenitor and neuronal development, driving the observed functional recovery following r6-MO treatment.

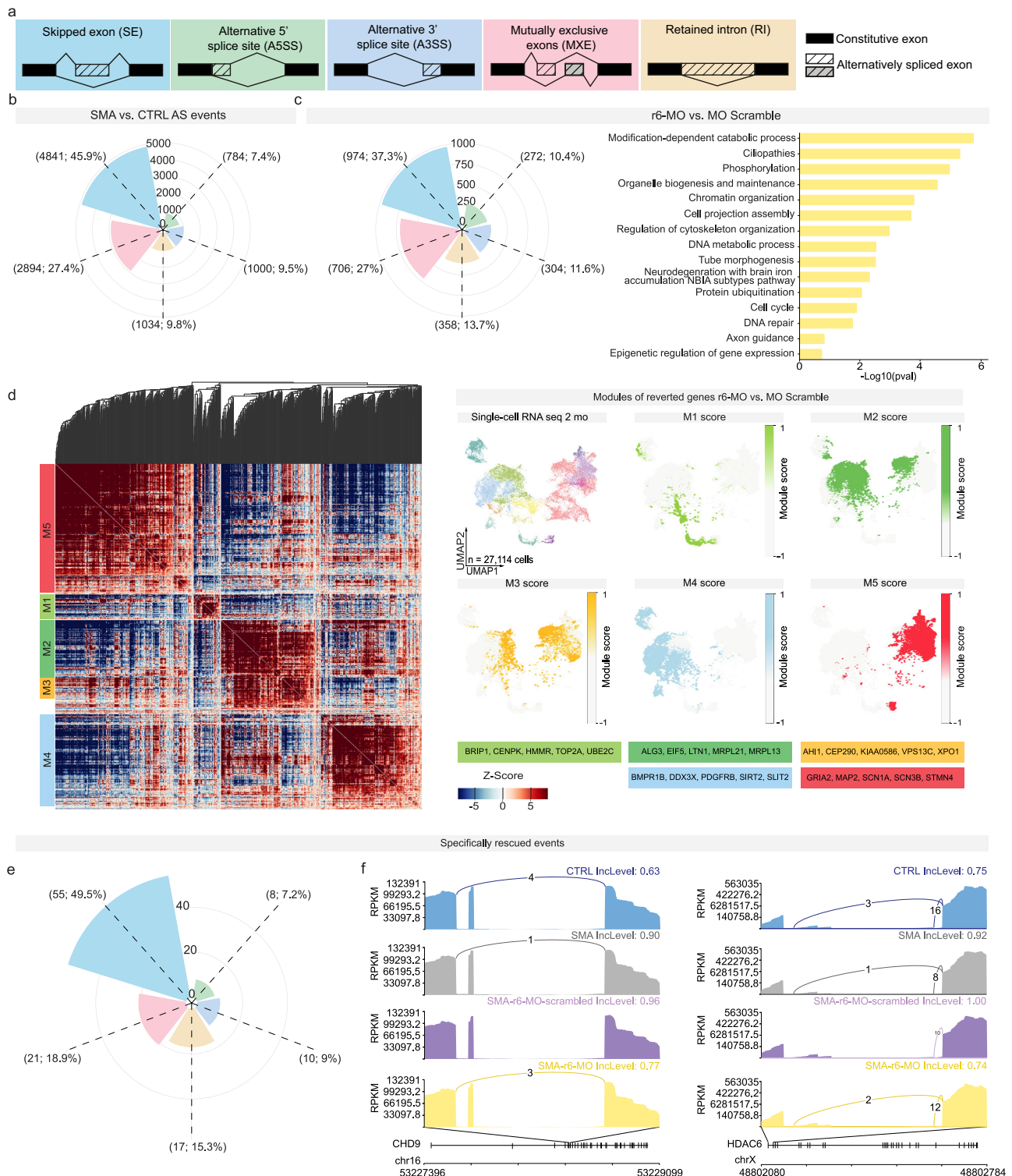


**Fig. 6 | r6-MO treatment modulates splicing events in SMA SCOs.** **a** Schematic of the main classes of alternative splicing events (AS). **b** Rose plot showing the frequencies of AS events, categorized by major event classes, based on a comparison between SMA vs. CTRL ( $n = 3$  C2,  $n = 3$  C3;  $n = 3$  S1,  $n = 3$  S2,  $n = 3$  S3). **c** Rose plot showing the frequencies of AS events, categorized by major event classes, based on a comparison between r6-MO vs. MO scrambled treatment in SCOs ( $n = 3$  S1,  $n = 3$  S2,  $n = 3$  S3). Gene Ontology, performed with Metascape, for the 1982 genes with an associated r6-MO specific splicing event. **d** Clustermap showing the single-cell co-expression profiles of 907 genes with splicing events specific to r6-MO at 2 months

in SMA single-cell RNA-sequencing, organized into distinct modules. Genes are grouped into modules based on shared co-expression profiles in low-dimensional space. Module scores are highlighted on the UMAPs of individual modules, with key genes highlighted for each module. **e** Rose plot showing the frequencies of AS events, categorized by major event classes, based on the overlap between the comparison SMA vs. CTRL and r6-MO vs. MO scrambled. These AS events are represented by those specifically reverted by r6-MO treatment in SCOs. **f** Sashimi plots display the read distribution and splice junctions for representative exon skipping events in *CHD9* and *HDAC6*, across the four experimental groups.

It is worth noting that the “reverted” genes, despite not showing any class-specific expression in our single-cell dataset, displayed significant enrichment in “SMA-S1 unmatched clusters”, which comprise both progenitors and neurons exclusively present in one of SMA patient (Supplementary Fig. 14e, f). Although confirmed only in one of the lines where these unmatched populations emerged, these data further suggest that an early splicing defect—caused by *SMNI* deficiency—could impact the molecular dynamic of spinal cord development, subverting the physiological trajectory of neuronal maturation and function.

Overall, these results point to a scenario in which the restoration of proper splicing landscape of genes associated with spinal cord development is among the key molecular events occurring upon MO treatment in SMA cells. This also suggests that in SMA organoids aberrant splicing dynamics impairs progenitor and neuron development and function, and that r6-MO induced splicing correction thus drives and/or contributes to the rescue of their cellular and functional phenotypes.

## Discussion

Stem cell-based models of the human CNS provide an opportunity to unravel processes of human biology that could not otherwise be studied experimentally<sup>41–43</sup>. Cerebral organoids have been proposed as a platform to study human brain development and identify disease phenotypes<sup>42,44–46</sup>. However, fewer descriptions of spinal cord-like organoids have been reported in the literature<sup>16,47–49</sup>, and this area of research deserves further investigation in the context of MN diseases, and neurological disorders with urgent unmet therapeutic needs. Here, we leveraged the organoid technology to generate SCOs and cerebral organoids from iPSCs of healthy subjects and SMA type 1 patients to further our understanding of SMA and test innovative optimized therapies.

The advent of disease-modifying therapies for SMA has changed the scenario of clinical practice and offered new expectations to patients, caregivers, and healthcare providers. Current evidence demonstrates that early treatment is essential for clinical efficacy. Thus, increased knowledge of the prenatal and pre-symptomatic stages of the disease is crucial to optimize therapeutic strategies. Even though SMA is a genetic disorder often with onset in newborns, very few studies have analyzed the prenatal stages of the disease, when SMN function is critical<sup>8</sup>, and no molecular data on human SMA spinal cord at single-cell resolution have been reported thus far, exploring how different cell populations are affected. Prenatal MN cell death and dysfunction might condition the onset and severity of the disease postnatally and set the therapeutic window. Still largely unexplored is whether SMN deficiency impairs early neuronal development and thereby triggers neuronal death. In this perspective, SMA organoids represent optimal substrates to begin addressing the link between key early pathological features. Here, we demonstrated that both CTRL and SMA SCOs harbor a spectrum of spinal neuronal domains recapitulating the *in vivo* complexity of neuronal populations within the human developing spinal cord (Fig. 1). Moreover, we showed that early differentiation programs are affected in SMA spinal organoids (Fig. 2) even before cell death becomes prominent. We identified the presence of a higher number of cells within the early developmental states in the SMA SCOs (Fig. 2). Despite the limitation of pseudotime inference based on a single time point, this analysis still offers meaningful insights into the altered developmental trajectory associated with SMA pathogenesis. These data, together with the pervasive molecular alterations observed in both progenitors as well as neuronal types at the same stage when cell death increases (2mo, Fig. 3), point towards an important developmental component in SMA pathogenesis and suggest that an aberrant developmental trajectory might negatively impact on the differentiation and survival of distinct neuronal subtypes.

While the developmental phenotype associated with SMA remained consistently detectable and statistically significant, even when analyses were performed within individual genotypes, a limitation of the SCO system is the variability in the representation of different cell populations across genotypes, and some differences in MN abundance between iPSC lines is to be acknowledged, especially in control lines. We recognize that performing analyses on iPSC lines derived directly from patients offers the advantage of working with patient-specific material, thereby encompassing broader biological variability. As a result, significant findings are more likely to be clinically relevant. On the other hand, the use of isogenic lines would allow a more precise attribution of phenotypic differences to the disease background rather than inter-individual variation, and therefore, this adds a potential limitation to our study. Nonetheless, despite these constraints, the developmental alteration emerged as a pervasive and biologically relevant phenotype. A recent parallel study modeled SMA using iPSC lines and their corresponding isogenic controls, generating SCOs containing both mesodermal and neural lineages<sup>49</sup>. Longitudinal single-cell transcriptomic analysis revealed impaired neural stem cell specification and a shift toward mesodermal and muscle progenitors, which represent developmental biases also observed in early SMA mouse embryos. These findings complement our results and aligns with the hypothesis that SMA pathogenesis is rooted in developmental processes, involving not only early fate restriction decisions but also broader neurodevelopmental defects that may contribute to later motor neuron degeneration. The developmental component of a neurodegenerative disorder such as Huntington’s disease has been recently studied<sup>50–52</sup> suggesting that this hypothesis can be investigated also in SMA.

The observation of reduced neurite length in SMA SCOs relative to CTRL demonstrates that the 3D model can reproduce key disease features of SMA (Fig. 3). Intriguingly, early neuronal differentiation defects and apoptosis were reproduced in SMA SCOs, suggesting that concomitant defects in differentiation and increased degeneration could contribute to SMA pathogenesis.

Interestingly, when we looked at DEG, we observed that a large fraction of them was detected in other cellular subgroups other than MNs. This data suggests that, despite defects of spinal MN function being the central feature of SMA pathology, the disease also has a broader impact. A growing body of evidence suggests that SMA is a multifactorial disease in which the interaction of different cell types and disease mechanisms progressively leads to MN dysfunction and death<sup>53,54</sup>. Magnetic resonance imaging has revealed that severe SMA patients who survive beyond 1 year of age exhibit progressive and diffuse brain lesions<sup>10</sup>. Prenatal spinal cord alterations have been reported in animal studies<sup>54</sup>, and recently in humans<sup>9</sup>. A very recent study demonstrated functional alterations of the motor cortex and cerebellum in symptomatic SMA mice<sup>55</sup>. Herein, we demonstrated that SMA cerebral organoids show impaired neuronal activity (Fig. 4). This wider impact requires further characterization and needs to be considered for the effective clinical management of SMA patients. Indeed, the generation of spontaneous and evoked activity in both SCOs and brain organoids is impaired (Fig. 4), demonstrating the biological relevance of the model and the direct impact that developmental alterations and/or plasticity events might cause on neuronal wiring. Neuronal hyperexcitability has been described in the context of SMA<sup>30,56</sup> and ALS<sup>57</sup>, associated with degeneration of both upper and lower MNs<sup>58,59</sup>. However, it is not clear how early in SMA progression this dysfunction arises and how it varies across CNS compartments. SMA SCOs showed decreased basal activity and hyperexcitability early on, likely contributing to the disease phenotypes. Furthermore, we reported an SMN-dependent deregulation of glutamate channel genes in multiple neuronal populations, which may point to intrinsic transcriptional changes in SMA neurons related to the observed hyperexcitability.

The last decade has witnessed the development of a growing number of available therapies for SMA. However, the FDA/EMA-approved treatment nusinersen<sup>60</sup>, an ASO able to increase SMN expression by splicing correction of *SMN2*, requires administration by periodic lumbar puncture. Permeability of the blood–brain barrier and tissue distribution of ASO delivery can be fostered by cell-penetrating peptides (CPPs), small cationic molecules with carrier capacity for macromolecular compounds. This strategy offers improved systemic distribution, including upon intravenous injection, in several disease models<sup>35</sup> and was proposed in the context of Duchenne muscular dystrophy<sup>61</sup>. In this current study, we tested the same conjugate in human tissue in SMA SCOs and demonstrated that the drug outperformed unconjugated MO in terms of increased SMN level and rescued SMA pathological hallmarks (Fig. 5).

We exploited deep sequencing bulk RNA-sequencing to globally analyze the altered splicing events in SMA organoids (Fig. 6). This allowed us to evaluate how splicing changes were present in different genetic backgrounds and how the SMN correction had a pervasive effect, independently of the patient-specific background, at the level of different cell types. Indeed, using single-cell RNA-sequencing data as a reference, we were able to assess how these rescued targets were expressed by different cell populations in varying developmental states and to uncover important molecular events related to spinal cord development in SMA pathogenesis. Here, we identified splicing alterations associated with SMA phenotype, whose correction might contribute to the rescue of key-pathological dysfunction.

This not only opens new avenues of investigation to fully dissect the therapeutic mechanisms of action on the multifaceted aspects of SMA, but also confirms these models as suitable tools to improve the current therapeutic strategies in the clinic, and even expand to more personalized medicine in the future. Altogether, our study suggests that SMN is a key molecule during prenatal spinal cord and brain development, meaning that SMA therapeutics will be most effective if delivered during the pre-symptomatic phase of the disorder, namely peri- or even prenatally. Further studies to analyze the multisystemic impact of SMN deficiency during development will be pivotal in defining the optimal therapeutic window and determining the efficacy of therapies on early developmental defects.

## Methods

The studies involving human samples were conducted in accordance with the ethical standards of the Declaration of Helsinki, national legislation, and institutional guidelines. Human fibroblast cell lines were obtained from Eurobiobank with informed consent, as approved by the ethical committee at Fondazione IRCCS Ca' Granda Ospedale Maggiore Policlinico and University of Milan (0004520).

### iPSC reprogramming and culture

Control iPSC lines C1 and C2 were derived from fibroblasts obtained from skin biopsies reprogrammed into iPSCs using the CytoTune iPS 2.0 Kit (CytoTune-iPS Sendai 2.0 Reprogramming Kit, Invitrogen). Control line C3 was obtained from Cedar Sinai CS5NXHICTR. Control line C4 was obtained from WiCell iPS DF 19-9-11 T.H and previously used in Corti et al.<sup>62,63</sup>. Control line C5 was previously generated from the Corti laboratory and published in Taiana et al.<sup>64</sup>. SMA line S1 was obtained from Cedars Sinai CS77iSMA. SMA line S2 was obtained from Cedars Sinai CS32iSMA. SMA line S3 was obtained from Cedars Sinai CS83iSMA. SMA line S4 was previously generated from the Corti laboratory<sup>65,66</sup>. SMA line S5 was previously generated from the Corti laboratory<sup>62</sup>. All iPSC lines were derived from male donors. iPSCs were maintained in E8 medium (Essential 8™ Medium, Gibco, A1517001) medium at 37 °C in 5% CO<sub>2</sub>.

### Embryoid bodies (EBs) formation

Embryoid bodies (EBs) were generated from iPSCs cultured in E8 medium (Essential 8™ Medium (Gibco, A1517001)) at 37 °C in 5% CO<sub>2</sub>. At ~80–85% confluency, iPSC colonies were detached using Collagenase IV at 2 mg/mL (Gibco, 17104019), collected, and gently resuspended in complete EB medium (DMEM/F12 (Gibco, 11320033), KnockOut Serum Replacement (Gibco, 10828028), MEM-NEAA Solution (Gibco, 11140035), 2-mercaptoethanol [55 mM] (Gibco, 21985023), GlutaMAX (Life Technologies, 35050061)) supplemented with bFGF at 4 ng/mL (Peprotech, 100-18B). Cells were transferred to non-treated tissue culture Petri dishes to promote suspension growth. EBs were maintained in suspension for up to 7 days, with medium changes (EB medium without bFGF) every other day following manufacturer's instructions (Pub. No. MAN0013784 Rev. 1.0).

### Generation of cerebral organoids (CrOs)

Cerebral organoids were generated by adapting a previous protocol<sup>14</sup>. Selected iPSCs were harvested using Accutase (Life Technologies, A1110501) and approximately 9000 iPSCs were plated in each well of an ultra-low attachment 96-well plate (Corning, CLS7007) in pluripotent stem cell media containing low recombinant human FGF-basic (4 ng/ml, Peprotech, 100-18B) and Y-27632 (50 μM ROCK inhibitor Calbiochem, 13624S). On day 6, obtained embryoid bodies (EBs) were transferred to low adhesion 24-well plates (Corning, CLS3473) in neural induction media (NIM) containing DMEM/F12 (Gibco, 11320033), 1% N2 supplement (Gibco, 17502001), 1% GlutaMAX (Life Technologies, 35050061), 1% MEM-NEAA (Gibco, 11140035), and 1 μg/ml heparin (Sigma, H3149). On day 12, the EBs were transferred to droplets of Cultrex® Basement Membrane Matrix Type 2 (BME type 2, Trevigen, 3532-001-02) and grown in differentiation media containing a 1:1 mixture of DMEM/F12 and Neurobasal (Gibco, 21103049) with 0.5% N2 supplement, 1% B27 supplement without vitamin A (Gibco, 12587010), 2-mercaptoethanol, 0.025% insulin (Sigma, I9278), 1% GlutaMAX, and 0.5% MEM-NEAA. After 2 days, the droplets were transferred to a spinning bioreactor containing the same media except for B27 without vitamin A, which was replaced with B27 with vitamin A (Gibco, 17504044). The speed of the spinning bioreactor was gradually increased up to 45 rpm.

### Generation of spinal cord organoids (SCOs)

To generate SCOs, the same procedure described for human cerebral organoids was applied from day 0 to day 2. On day 2, half of the medium was changed to fresh medium containing a final concentration of 4 ng/ml bFGF (Peprotech, 100-18B), 50 μM Y-27632 (ROCK inhibitor Calbiochem, 13624S), 3 μM CHIR 99021 (GSK3 inhibitor, Sigma-Aldrich, SML1046), 2 μM SB-431542 (Activin/BMP/TGF-β pathway inhibitor, Sigma-Aldrich, S4317), and 0.2 μM LDN-193189 (inhibitor of the bone morphogenetic protein [BMP] pathway, Stemcell Technologies, 72149). On day 4, the medium was replaced, adding the same small molecules (excluding bFGF and Y-27632). On day 6, the EBs were transferred into ultra-low attachment 24-well plates and cultured in NIM plus 100 nM retinoic acid (RA, Sigma-Aldrich, R3255). On day 12 EBs embedded in Cultrex and cultured with SCO differentiation media (SCODM, composed of 1:1 DMEM/F12 and Neurobasal with 0.5% N2 supplement, 1% B27, 2-mercaptoethanol, 0.025% insulin (Sigma, I9278), 1% GlutaMAX, and 0.5% MEM-NEAA). 1 μM Smoothed Agonist (SAG, Calbiochem, 364590-63-6) was added to the media. On day 14, SCOs were transferred to spinning bioreactors and cultured with SCODM supplemented with RA and SAG. On day 28, concentrations of RA and SAG were reduced to 50% and neurotrophic factors BDNF (Peprotech, 450-02), GDNF (Peprotech, 450-10), and IGF-1 (Sigma-Aldrich, 100-12) were added at 10 ng/ml each.

### Immunohistochemistry analysis

Organoids were fixed with 4% paraformaldehyde (PFA) for 15 min at room temperature (RT) and subsequently placed in 30% sucrose/1× PBS overnight at 4 °C. The next day, they were embedded in 10%–7.5% gelatin/sucrose, frozen in dry ice, placed at –80 °C overnight, and cryosectioned into 20- $\mu$ m sections using a cryostat. Organoid sections were permeabilized for 1 h in 1× PBS with 0.3% Triton-X (Sigma) and 10% donkey or goat serum (Jackson ImmunoResearch) at RT. 2D cultures were fixed with 4% PFA at RT for 5 min and permeabilized in 1× PBS with 0.2% Triton-X (Sigma) and 10% donkey or goat serum (Jackson ImmunoResearch) for 1 h at RT. Primary antibody diluted in fresh permeabilization solution was added overnight at 4 °C (complete list summarized in Supplementary Data 2). The following day, secondary antibodies (AlexaFluor 488, 555, 568, 594, and 647 conjugates, 1:1000; Invitrogen) were added with DAPI (1:500; Sigma-Aldrich, D9542) in 1× PBS for 90 min at RT. DAKO mounting media (Agilent, S3023) was used to mount the coverslips. TUNEL assay was performed using a Dead-End™ Fluorometric TUNEL System (Promega, G3250). Confocal images were obtained using a Leica SP8 white laser inverted confocal microscope (Leica) and analyzed using Fiji image-processing software.

### Image quantification

To evaluate the number of SOX2<sup>+</sup> cells and the percentage of TUJ1-positive area, 10× mosaic images of whole SCOs sections were acquired using an Inverted Microscope DMI8 and the Leica LASX software platform. 20× mosaic images of whole brain organoid sections were imaged using Zeiss Axio Microscope and the Zen Light software platform. At least three different sections were acquired per organoid for at least 3 organoids/cell lines for  $n > 3$  CTRL and SMA lines (Supplementary Data 1). In detail, to compute the number of SOX2<sup>+</sup> cells, a custom-written Cell Profiler<sup>67</sup> pipeline was designed, and a custom-designed ImageJ/Fiji<sup>68</sup> software image macro was applied to evaluate the proportion of TUJ1<sup>+</sup> area (as %). For TUNEL quantification, images were acquired by an inverted Nikon-Crest multimodal spinning-disk confocal microscope. Quantification of nuclei (DAPI) and TUNEL-positive cells was performed with an ad-hoc designed analysis pipeline for thresholding and segmentation using the GA2 module in NIS-Elements v5.21 software (Nikon-Lim Instruments). Regarding neurofilament tracing, images previously acquired with a Leica SP8 white laser inverted confocal microscope (Leica) were analyzed using Fiji image-processing software. The NeuronJ plug-in was used for the tracing and analysis of neurite length; only filaments that both originated and terminated within the field of view were traced. Filaments extending beyond the field of view or those for which the origin could not be determined were excluded from consideration.

### Quantitative real-time PCR (qRT-PCR)

Total RNA was extracted using the ReliaPrep RNA Cell Miniprep System (Promega, Z6010). The RNA concentration was tested using Nanodrop (Thermo Fisher Scientific). Reverse transcription was performed using SuperScript IV VIL0 Master Mix (Thermo Fisher Scientific, 11756500). 150 ng of template total RNA were retrotranscribed. This protocol has been used to process bulk RNA samples. The expression level of candidate genes (Supplementary Data 3) was assessed by: (i) TaqMan quantitative analysis on the 7500 Real-Time PCR System and 7900HT Fast Real-Time PCR System (Applied Biosystem), GAPDH was used as a reference gene; (ii) PowerTrack SYBR (Thermo Fisher Scientific) quantitative analysis on the ViiA 7 Real-Time PCR System (Thermo Fisher Scientific), ACTB was used as a reference gene.

### FL and $\Delta 7$ transcript analysis

Total RNA extracted from iPSC or SCOs were retrotranscribed using the SuperScript IV VIL0 Master Mix (Thermo Fisher Scientific). The

relative expression levels of FL and  $\Delta 7$  transcripts were assessed by RFLP analysis of RT-PCR products (primers available upon request). PCR products underwent o/n digestion at 37 °C by DdeI endonuclease, followed by electrophoresis on a 2.5% agarose gel. DdeI recognizes and cuts molecules containing the *SMN2* exon 8, allowing the discrimination of the genomic origin (*SMN1* or *SMN2*) of FL and  $\Delta 7$  isoforms.

### Electrophysiology

HD-MEA was used to record the extracellular spontaneous activity of both SCOs and cerebral organoids. The device consists of 4096 planar electrodes measuring 21 × 21  $\mu$ m, covering an area of 2.67 × 2.67 mm (Biocam X with Biochip Arena, 3Brain AG, Switzerland). Organoids were gently positioned on the chip and fixed with a platinum anchor and with a nylon mesh. Before and during recordings, organoids were submerged in Krebs's solution with the following composition (mM): 120 NaCl, 2 KCl, 1.19 MgSO<sub>4</sub>, 26 NaHCO<sub>3</sub>, 1.18 KH<sub>2</sub>PO<sub>4</sub>, 11 glucose, 2 CaCl<sub>2</sub>, oxygenated with a mix of 95% O<sub>2</sub>/5% CO<sub>2</sub> to obtain pH 7.4. Organoids were recorded under control conditions for 15 min, after addition of 100  $\mu$ M of glutamate (L-glutamic acid, Sigma-Aldrich) for an additional 15 min, and after adding the combination of 100  $\mu$ M glutamate, 10  $\mu$ M gabazine (SR-95531, Abcam), and 1  $\mu$ M strychnine hydrochloride (Sigma-Aldrich) for an additional 15 min. Brainwave X (3Brain AG) software was used to record the electrophysiological activity at the sampling frequency of 17 kHz. Brainwave 4 software (3Brain AG) was used to analyze the traces offline. The precise time spike detection algorithm was used to detect the spikes (parameters used: positive and negative peak, peak duration <1 ms, refractory period >1 ms, and detection threshold >7 times the standard deviation of the noise). Spike sorting was performed using a principal component analysis with K-means (silhouette method) considering a maximum three clusters per electrode and three spikes per cluster. The Pakhira-Bandyopadhyay-Maulik index was used for validating clustering results<sup>69</sup>. A final checkout was performed by the researcher by re-analyzing the signals and removing any confounders. Only channels showing stable activity during the control period (without spike frequency fluctuations exceeding 20% spike frequency) were taken into consideration. The number of channels per organoid considered for the analysis was comparable between control (SCO 13.6 ± 0.6; cerebral 13.8 ± 2.1), SMA (SCO 15.2 ± 0.7; cerebral 15.4 ± 0.9), and treated SMA (SCO 12.8 ± 1.3) organoids. The percentage change in basal firing frequency was calculated by comparing the average firing frequency in the last 10 min before glutamate addition with the interval between 5 and 15 min after glutamate addition.

### Morpholino treatment

We used a morpholino (MO-10–34) sequence targeting the *SMN2* ISS-N1 region downstream of exon 7 that was previously described by our lab<sup>34</sup>. The specific MO sequence designed to target *SMN2* pre-mRNA was GTAAGATTCACCTTCATAATGCTGG. The CPP used in the study is r6 (RRRRRR, D enantiomeric configuration), which was covalently conjugated to the 5' end of the MO by our external collaborator, Dr. Hong Moulton. A scramble MO (scr, GTAACATTGACTTTGATATTCCTGG) was used as a control for antisense specificity. We used MO alone and conjugated with r6 peptide (r6-MO)<sup>36</sup>. As a negative control, we used a custom-made r6-MO containing the scrambled sequence. To assess biodistribution, we used a biotinylated r6-MO that was added to the culture medium as described below. All MO oligomers were synthesized by Gene Tools. We treated SMA SCOs with increasing concentrations of MO or r6-MO. The solution containing 2.4 nmol MO or r6-MO was added directly to each well and incubated for 48 h. Afterward, the culture medium was changed and fresh aliquots of 2.4 nmol MO or r6-MO were added for an additional 48 h. The medium was then replaced with fresh medium for 72 h. Lastly, the organoids were treated again with 4.8 nmol of MO or r6-MO for 48 h.

## Western blot analysis

Western blot analysis was performed as described previously<sup>34</sup>. Briefly, samples were sonicated in lysis buffer supplemented with protease and phosphatase inhibitors (Pierce Rockford, IL, USA) on ice for 10 min. Approximately 25 µg of protein was separated by 12% SDS-PAGE and electrophoretically transferred to a nitrocellulose membrane. The membranes were incubated with anti-SMN (1:1000, BD) and anti-actin (1:1000, Sigma, St. Louis, MO, USA) antibodies. After labeling with peroxidase-conjugated secondary antibody (Life Technologies), the proteins were detected using a chemiluminescent substrate (Amersham, Pittsburgh, PA, USA). Signal was detected using LI-COR Odyssey 9120. Densitometry analysis was performed using Image Studio Lite (v5.2).

## 2D culture of cells from dissociated organoids

SCOs were centrifuged at 300 × *g* for 5 min and trypsin-EDTA was added before transferring the organoids to a 37 °C water bath for 5 min. The organoids were then mechanically dissociated, and a double volume of horse serum (Euroclone, ECS0091L) was used to inactivate the trypsin before centrifugation. The supernatant was discarded, and SCO differentiation medium was employed to resuspend the pellet. Approximately 50,000 cells were seeded in 24-well plates with coverslips previously coated with poly-L-ornithine (Sigma-Aldrich, P3655) and laminin (Sigma-Aldrich, L2020). SCODM supplemented with RA, SAG, and growth factors at the same concentration of differentiation day 28, was used for the maintenance of organoid-derived cells.

## Whole mount staining

Organoids were washed in 1× PBS and then fixed in 4% PFA on a spinning wheel at 4 °C overnight. The following day, five 1× PBS washes (10 min each) were performed on the spinning wheel at RT. Organoids were permeabilized with 0.25% Triton ×-100 in 1× PBS for 15 min. To prevent non-specific binding, organoids were incubated in 1× PBS with 10% FBS and 0.5% serum. Primary antibodies were replaced three times (after 2, 12, and 5 h) and were diluted in 1× PBS with 5% FBS, 0.5% serum of the same species as the primary antibodies, and 0.1% Triton ×-100. Secondary antibodies were diluted in the same solution used for primary antibodies and incubated overnight at RT on the spinning wheel. Images were acquired using a Nikon's A1 R MP+ multiphoton microscope by the Alembic Facility (IRCCS Ospedale San Raffaele).

## SCO cell dissociation for single-cell RNA-sequencing analysis

Organoids were dissociated using an optimized protocol based on the Worthington Papain Dissociation System Kit (Worthington Biochemical). Single cell suspensions were collected on ice-cold 1× PBS (without calcium and magnesium) with 0.04% BSA (Sigma-Aldrich) at 1 × 10<sup>6</sup>/ml as counted by an automatic cell counter (Countess II, Thermo Fisher).

## Single-cell RNA-sequencing and downstream analysis

Sample processing. Approximately 8000 cells from each sample, prepared as described above were loaded into one channel of the Single Cell Chip B using the Single Cell 3' v3 reagent kit (10× Genomics) for gel bead emulsion generation in the Chromium system. Following capture and lysis, cDNA was synthesized and amplified for 14 cycles following the manufacturer's protocol (10× Genomics). The amplified cDNA (50 ng) was then used for each sample to construct Illumina sequencing libraries. Sequencing was performed on the NextSeq550 Illumina sequencing platform following the 10× Genomics instructions for read generation. A sequencing depth of ~45,000 reads/cell was obtained for each sample.

Data analysis. Raw sequencing data (bcl-files) were converted to fastq files using the Illumina bcl2fastq tool integrated into the Cell Ranger (10× Genomics) suite (*v* = 3.0.2). The Cell Ranger analysis pipeline was used to generate a digital gene expression matrix starting

from raw data. Reads were aligned to the human GRCh38 reference genome, annotated, and counted with gene annotations from Ensembl version 93. The Cell Ranger count module was used to map reads with default settings, and the sequence length was set to *r1-length* = 28 and *-r2-length* = 55. At least 90,000 reads per cell were produced. For further preprocessing and analysis, we used the Scanpy<sup>70</sup> single-cell analysis toolkit (*v* = 1.9.6, pandas *v* = 2.2.0, and numpy *v* = 1.26.3). Doublets were identified and removed with Scrublet<sup>71</sup> (*v* = 0.2.3). The threshold at doublet scores was automatically set by the Scrublet algorithm and was used individually for each sample. Quality control metrics, including mitochondrial and ribosomal content, were calculated using *sc.pp.calculate\_qc\_metrics* function, and then the object was filtered for the outliers cells containing less <10% mitochondrial and <5% ribosomal transcripts. Further, cells were filtered using a sample-specific median absolute deviation (MAD) threshold of “*n\_genes\_by\_counts*”. After filtering, the data were concatenated using *sc AnnData.concatenate*, annotated with sample names and genotypes. We used *scVI-tools*<sup>72</sup> (*v* = 1.1.0) to mitigate batch effects where each genotype and sample was treated as a batch. The *AnnData* object was first transformed by copying counts to *adata.layers[“counts”]* and identifying 2000 highly variable genes using *sc.pp.highly\_variable\_genes* with the Seurat V3 flavor, considering the “Sample” batch key. The transformed data were prepared for scVI analysis by setting up *AnnData* with categorical covariates “Sample” and “genotype”, and continuous covariates “*pct\_counts\_mt*”, “*pct\_counts\_ribo*”, and “*total\_counts*”. The scVI model was initialised with *scvi.model.SCVI* and trained using default parameters. The latent representation was extracted using *model.get\_latent\_representation* and stored in *adata.obsm[“X\_scvi”]*. Dimensionality reduction was performed by constructing a KNN graph with *sc.pp.neighbors* using the latent representation (*X\_scvi*) and running UMAP with *min\_dist* = 0.2. Clustering was executed at resolutions 0.25, 0.3, 0.5, 0.7, and 1.0 using the Leiden algorithm<sup>73</sup> (*sc.tl.leiden*), and the results were visualized with UMAP plots (*sc.pl.umap*) displaying cluster assignments, sample information, and genotype. After integration, the data were reverted to all genes using *adata.raw.to\_adata()*. Raw counts were normalized using *sc.pp.normalize\_total(adata, target\_sum = None, inplace = False)* and log-transformed with *sc.pp.log1p* as suggested in the recent sc-RNA-seq data transformation benchmark study<sup>74</sup>. The final processed data were saved for downstream analysis. Gene set scores were calculated using Scanpy's *sc.tl.score\_genes* function. To find DEG, we applied the Wilcoxon rank-sum test on the normalised counts between all found clusters (resolution = 0.7), the top 50 genes sorted by the *p*-value and log-fold change were considered for the biological interpretation.

Differential abundance testing. We performed differential abundance testing using the Python version of Milo<sup>25</sup> (*v* = 0.1.1). Neighborhoods were constructed with a proportion of 0.1 using *milo.make\_nhoods*. Neighborhood counts were computed with *milo.count\_nhoods* using the sample column “Sample”. Both genotypes (CTRL and SMA) were encoded as continuous and categorical variables. Differential abundance testing was conducted using *milo.DA\_nhoods* with a design formula based on genotype. A neighborhood graph was built using *milopy.utils.build\_nhhood\_graph* and visualized with *milopy.plot\_nhhood\_graph*, highlighting the spatial false discovery rate (FDR) at 1%. Neighborhoods were annotated with cell types using *milopy.utils.annotate\_nhoods* and the color palette from Leiden clustering was mapped to the neighborhoods.

Pseudo-bulk differential gene expression analysis between SCOs genotypes. To test for DEG between genotypes for a particular cell identity (at least 25% of cell proportion for each genotype), we leveraged the PyDESeq2<sup>75</sup> (*v* = 0.4.4) and the Python implementation of decoupleR<sup>76</sup> packages (*v* = 1.6.0). Pseudo-bulk profiles were generated using the *decoupler.get\_pseudobulk* function with a minimum of 10 cells and 1000 counts per group. The pseudo-bulk data were

normalized, log-transformed, scaled, and principal component analysis (PCA) was performed. Associations between metadata and principal components were computed using `decoupler.get_metadata_associations`, and the results were visualized with `decoupler.plot_associations`. Data were subset by cell type, and differential expression analysis was performed on selected cell types. Genes were filtered by expression with a minimum count of 10 and a minimum total count of 15. The DESeq2 object was constructed with the design factor “genotype” and reference level “CTRL”. Log fold changes (LFCs) were computed, and contrasts between SMA and CTRL genotypes were extracted. DEG were filtered by adjusted  $p$ -value ( $<0.05$ ) and absolute LFC ( $>0.5$ ). The results then were visualised in the form of complex heatmaps and volcano plots with custom R scripts. The lists of DEG of selected cell types was analyzed using the Ingenuity Pathway Analysis (IPA—Qiagen Ingenuity Systems) to compute canonical pathways and biological functions enrichment.

**Prediction of SCOs differentiation states and pseudotime analysis.** We performed the prediction of developmental potential on the integrated data using CellRank’s<sup>77</sup> ( $v=2.0.0$ ) implementation of CytoTRACE<sup>78</sup>. The data were preprocessed by ensuring availability of spliced and unspliced RNA counts, with these layers established from the primary expression matrix when missing. Moments of spliced and unspliced abundances were computed using `scvelo.pp.moments`. Lately, the CytoTRACE kernel from CellRank was applied to calculate the CytoTRACE score and construct a corresponding transition matrix. CytoTRACE pseudotime was derived from the computed scores to quantitatively represent cellular differentiation status. Pseudotime scores were visualized as density plots comparing different genotypes. Density distributions were estimated using Gaussian kernel density estimation (`scipy.stats.gaussian_kde`) and plotted as ridgeline plots, color-coded by genotype and cell type. Visualization and figure customization were performed using the Matplotlib library in Python. To statistically compare pseudotime distributions between genotypes (CTRL vs. SMA), a two-sided KS test was performed using SciPy’s `ks_2samp` function. Pseudotime values for each genotype were extracted, and the KS statistic and associated  $p$ -value were computed to assess differences in distribution between groups.

**Regulons inference and trajectory analysis of motoneurons lineage.** To infer the co-expression modules between transcriptional factors and putative target genes in MN cell lineage, we used the pySCENIC ( $v=0.12.1$ ) pipeline<sup>28</sup>. We performed independent pipeline runs for each SCOs genotype data object with the Singularity container. At the first step of regulons inference, the pipeline relies on a machine learning model that fits the expression patterns of genes to expression patterns of TFs by the GRNBoost2<sup>79</sup> algorithm. For this part, we used the command line tool (`pyscenic:0.12.1 arborito_with_multiprocessing.py`) with the default parameters. Next, the output fits were used to predict the potential regulons and direct-binding targets that are then refined through TFs motifs enrichment analysis with (`pyscenic:0.12.1 pyscenic ctx`) with “-maks dropout” parameter. Lastly, cells were scored for each regulon activity in SMA and CTRL objects, respectively via the AUCell method<sup>80</sup> with (`pyscenic:0.12.1 pyscenic aucell`). Obtained regulons activities scores and metadata were used in the secondary analysis for visualisation and trajectory analysis. We performed trajectory analysis on SCOs focusing on motoneuron lineage using Palantir<sup>81</sup> ( $v=1.3.3$ ) and scFates<sup>82</sup> ( $v=1.1.1$ ). The SCOs data object was loaded, and specific clusters unrelated to the MN lineage were removed. Diffusion maps were computed to generate a multiscale diffusion space with four eigenvectors. The principal tree was constructed using `scf.tl.tree` with parameters `method="ppt"`, `Nodes=200`, `ppt_lambda=100`, `ppt_sigma=sig`, `ppt_nsteps=200`. The root was set to the SOX2 expression using `scf.tl.root` and corresponded to the pMN. Later, the pseudotime was computed using `scf.tl.pseudotime` with `n_jobs=20`, `n_map=50`, `seed=42`. To explore the differences in motoneuron differentiation along a shared

trajectory, the data were stratified by genotype into CTRL and SMA MN groups. For each group, dendrograms were generated using `scf.pl.dendrogram` and KDE plots (`seaborn.kdeplot`). Next, the pySCENIC AUCell output was processed to align with the motoneuron trajectory data generated before and this approach was adopted from the study of Petitpré C et al.<sup>83</sup>. pySCENIC AUCell output for control and SMA samples was loaded from `loom` files. The AUCell matrices were aligned with the trajectory data by matching cell IDs. Regulons active in fewer than six cells were filtered out. Regulon activity was tested for association with trajectory data using `scFates` and GAM (`scf.tl.test_association` with `n_jobs=20` and `A_cut=0.025`). Pseudotime for cells was updated based on their order in trajectory analysis (`adata.uns["pseudotime_list"]`), and the trajectory model was fitted (`scf.tl.fit` with `n_jobs=20`). The trend of specific regulons activity along the trajectory segments was visualised using `scf.pl.single_trend` and `scf.pl.trends`. For control samples, a set of significant regulons was highlighted, and the trends of these regulons were plotted. Similar analyses were performed for SMA samples.

**Identification of informative splicing gene modules.** To associate splicing gene modules to clusters in the SCOs object (CTRL or SMA), we subsetted the object to contain only the selected pools of splicing genes, but all cells. Using scVI dimensionality reduction, Hotspot<sup>84</sup> ( $v=1.1.1$ ) analysis was conducted to identify gene modules by calculating autocorrelations for the genes and identifying significant genes with an FDR  $<0.05$ . Local correlations were computed for the significant genes using 15 parallel jobs, and gene modules were created with a minimum gene threshold of 50, core-only mode, and an FDR threshold of 0.05. Module scores were calculated and assigned to the dataset. Finally, module scores of splicing genes were visualised using scatter plots on UMAP coordinates with custom color palettes.

**Stage mapping to reference fetal spinal cord data.** To map our control organoid dataset onto a temporal developmental reference, we first processed a fetal spinal cord single-cell atlas<sup>23</sup> using Scanpy. After standard cell and gene filtering, the data was normalized, and 2000 highly variable genes (HVGs) were identified using a batch-aware “seurat\_v3” approach. We then trained a four-layer scVI model on these HVGs to create a latent reference space. Our control organoid query data was subsequently aligned to this 2000-gene set by adding missing genes with zero expression. Using the scArches ( $v=0.6.1$ ) package projected the query data onto the reference atlas via partial model retraining. The developmental stage of CTRL organoid cells was then inferred by transferring “Gestational Week” and “Trimester” labels from the atlas using a weighted-kNN classifier ( $k=100$ ), and we quantified the similarity between query and reference states by calculating cell presence scores.

**Cell types mapping to reference fetal spinal cord data.** First, the raw count matrix of fetal spinal cord atlas<sup>24</sup> was loaded from a `h5ad` file into an `AnnData` object. The raw counts were preserved in a separate layer, after which the data was normalized to a total of 10,000 counts per cell (`normalize_total`) and subsequently log-transformed (`log1p`). The top 2000 highly variable genes were identified across batches using the `seurat_v3` method on the raw count layer, with the dataset being subset to these genes. To correct for batch effects associated with developmental stages, we employed the scVI-tools package ( $v=1.3.0$ ). The model was set up using the raw counts and the stage annotation as the batch key. The scVI model was initialized with two hidden layers and trained to learn a latent representation of the cells. This latent space embedding was then used as the basis for semi-automatic annotation. To assign broad cell identities, gene module scores were calculated based on marker genes adapted from ref. 24. These scores enabled the classification of major tissue types, including spinal cord progenitor, spinal cord neuron, sensory neuron/progenitor, mesoderm, hematopoietic, and erythrocytes, as visualized in ref. 24.

Reference model pre-training. A pre-processed and annotated fetal spinal cord dataset was used for scPoli<sup>85</sup> model training, a deep generative model designed to integrate datasets from different conditions while preserving cell type identity. We first identified the top 2000 highly variable genes (HVGs) across experimental batches (stage key) using the *seurat\_v3* method. The scPoli model was initialized on the data subset containing only the HVGs. The model was configured using stage as the condition key and manually assigned cell types as the cell type key. The architecture was defined with a 32-dimensional latent space and a single hidden layer of 1024 nodes. A Zero-Inflated Negative Binomial loss function was used for data reconstruction. The model was trained for a maximum of 50 epochs, with 40 pre-training epochs and an early stopping mechanism which monitored the validation prototype loss with a patience of 10 epochs. Upon completion of training, the learned latent representation was extracted and stored in the original AnnData object. This integrated “X\_scPoli” embedding was then used for transfer learning and downstream analysis, including the computation of a k-nearest neighbor graph and visualization with UMAP. To compare our spinal cord organoid dataset with an in vivo reference, we performed computational mapping using a pre-trained scPoli model built on fetal spinal cord atlas. First, the query organoid dataset was loaded, and cells from control (CTRL) samples were isolated for the analysis. To ensure compatibility with the reference model, the query data’s gene set was aligned to the 2000 highly variable genes used to train the reference. Genes present in the reference but absent from the query were added with zero-count expression values. We utilized an scArches<sup>86</sup> ( $v = 0.6.1$ ) workflow to project the query data into the reference latent space. The mapping was performed using a partial retraining strategy (retrain = “partial”) for 30 epochs, which fine-tunes the model on the query data while keeping the reference cell embeddings fixed. Following the mapping, we constructed a weighted k-nearest neighbor (wknn) graph in the shared latent space, connecting each query cell to its  $k = 100$  nearest neighbors in the reference atlas with HNOCA-tools package<sup>87</sup> ( $v = 0.1.1$ ). This graph formed the basis for label transfer, where cell type annotations from the reference were assigned to each organoid cell, yielding the final labels and a quantitative confidence score. The resulting latent space coordinates and transferred annotations were then added back to the original query object for further analysis. Secondly, we calculated cell presence scores for primary tissue to quantify the compositional similarity between the organoid sample and the fetal reference atlas. The resulting latent embedding and annotations were added to the query object for downstream visualization and analysis.

### Bulk RNA-seq analyses

**Library construction.** Libraries were prepared starting from 50 ng of total RNA derived from 9 control, 6 SMA, and 16 morpholino-treated SMA (8 r6-MO, 8 r6-MO-scrambled) organoids, using the SMARTer Stranded RNA-Seq Kit, TaKaRa) and following the manufacturer’s instructions. Samples underwent a high coverage paired-end 150-bp strand-specific sequencing using a NextSeq 2000 platform (Illumina).

**Alignment.** For each sample (9× control organoids, 6× SMA organoids, 8× SMA organoids treated with r6-MO, and 8× SMA organoids treated with r6-MO-Scramble), raw reads were mapped to the human hg38 genome and counted using STAR v2.7.10a<sup>88</sup>.

**SMN1 and SMN2 counts.** *SMN1* (SMN-C) and *SMN2* (SMN-T) genes are characterized by a very high degree of homology (more than 99%). Thus, to distinguish the reads derived from the two genes, we counted the number of reads mapping to exon 7, where the presence of a nucleotide difference between the two genes enables their unambiguous identification. We performed this check using the IGV tool. Counts mapping elsewhere on the *SMN* genes were not considered for this analysis.

**Differential gene expression analysis.** Differential gene expression analysis was carried out using R and the edgeR package v4.0.2 with the functions *estimateDisp*, *glmFit*, and *glmLRT*. Genes having *cpm* < 0.05 in at least 6 samples were filtered out.

**Gene ontology differential expressed genes.** Gene ontology of differential expressed genes between CTRL and SMA organoids was done using Ingenuity Pathway Analysis. Terms from “Canonical pathways” and “diseases and functions” were filtered.

**Differential splicing analysis.** Differential splicing analysis between samples was determined using rMATS turbo v4.3.0<sup>89</sup>, a tool that identifies 5 basic types of AS patterns: SE, MXE, alternative 5’ (A5SS) and 3’ splice sites (A3SS), and retained introns (RI). Significant events were characterized by a *FDR* < 0.05 and an absolute Inclusion Level Difference > 0.05. Only the reads mapping to exon-exon junctions were used for the analyses. Sashimi plot of events of interest were created using *rmats2sashimiplot* v2.0.4 (<https://github.com/Xinglab/rmats2sashimiplot>).

**Gene ontology of splicing events.** Differential splicing events from SMA vs. CTRL and SMA r6-MO vs. SMA r6-MO-Scrambled were compared. Events sharing (i) the same starting position and the same ending position and (ii) with opposite Inclusion Level Difference were called as “common events”. To annotate gene function, gene ontology was performed using Metascape<sup>90</sup>. Downstream processing of splicing and gene expression data were done in R v4.1.0 using custom scripts.

### Statistical analysis

Continuous variables were reported as mean ± SD. Comparisons between groups and between baseline and post-intervention or interval within a group were assessed using unpaired and paired two-sided Student’s *t*-test, respectively. One-way or two-way ANOVA was used for comparisons among groups, with Tukey HSD or Sidak’s post-hoc tests applied when the null hypothesis for the omnibus analysis was rejected. GraphPad Prism v.8 was used for all analyses with a significance level of 0.05.

### Reporting summary

Further information on research design is available in the Nature Portfolio Reporting Summary linked to this article.

### Data availability

All data are available in the main text or the supplementary materials. Source data are provided with this paper. Read-level data from scRNA-seq have been deposited at [GSE290980](https://www.ncbi.nlm.nih.gov/bioproject/1000000000) while count-level data and metadata from bulk RNA-seq have been deposited at [GSE290979](https://www.ncbi.nlm.nih.gov/bioproject/1000000000). Source data are provided with this paper.

### References

1. Kolb, S. J. et al. Natural history of infantile-onset spinal muscular atrophy. *Ann. Neurol.* **82**, 883–891 (2017).
2. Faravelli, I., Nizzardo, M., Comi, G. P. & Corti, S. Spinal muscular atrophy—recent therapeutic advances for an old challenge. *Nat. Rev. Neurol.* **11**, 351–359 (2015).
3. Lorson, C. L., Hahnen, E., Androphy, E. J. & Wirth, B. A single nucleotide in the SMN gene regulates splicing and is responsible for spinal muscular atrophy. *Proc. Natl. Acad. Sci. USA* **96**, 6307–6311 (1999).
4. Parente, V. & Corti, S. Advances in spinal muscular atrophy therapeutics. *Ther. Adv. Neurol. Disord.* **11**, 1756285618754501 (2018).
5. Mercuri, E., Pera, M. C., Scoto, M., Finkel, R. & Muntoni, F. Spinal muscular atrophy - insights and challenges in the treatment era. *Nat. Rev. Neurol.* **16**, 706–715 (2020).

6. Mercuri, E., Sumner, C. J., Muntoni, F., Darras, B. T. & Finkel, R. S. Spinal muscular atrophy. *Nat. Rev. Dis. Prim.* **8**, 1–16 (2022).
7. Soler-Botija, C., Ferrer, I., Gich, I., Baiget, M. & Tizzano, E. F. Neuronal death is enhanced and begins during foetal development in type I spinal muscular atrophy spinal cord. *Brain* **125**, 1624–1634 (2002).
8. Ramos, D. M. et al. Age-dependent SMN expression in disease-relevant tissue and implications for SMA treatment. *J. Clin. Invest.* **129**, 4817–4831 (2019).
9. Kong, L. et al. Impaired prenatal motor axon development necessitates early therapeutic intervention in severe SMA. *Sci. Transl. Med.* **13**, eabb6871 (2021).
10. Mendonça, R. H. et al. Severe brain involvement in 5q spinal muscular atrophy type O. *Ann. Neurol.* **86**, 458–462 (2019).
11. Faravelli, I., Costamagna, G., Tamanini, S. & Corti, S. Back to the origins: human brain organoids to investigate neurodegeneration. *Brain Res.* **1727**, 146561 (2020).
12. Tiziano, F. D. & Tizzano, E. F. 25 years of the SMN genes: the Copernican revolution of spinal muscular atrophy. *Acta Myol.* **39**, 336–344 (2020).
13. Tizzano, E. F. et al. Outcomes for patients in the RESTORE registry with spinal muscular atrophy and four or more SMN2 gene copies treated with onasemnogene abeparvovec. *Eur. J. Paediatr. Neurol.* **53**, 18–24 (2024).
14. Lancaster, M. A. et al. Cerebral organoids model human brain development and microcephaly. *Nature* **501**, 373–379 (2013).
15. Velasco, S. et al. Individual brain organoids reproducibly form cell diversity of the human cerebral cortex. *Nature* **570**, 523–527 (2019).
16. Andersen, J. et al. Generation of functional human 3D cortico-motor assembloids. *Cell* **183**, 1913–1929.e26 (2020).
17. Ma, X. R. et al. TDP-43 represses cryptic exon inclusion in the FTD-ALS gene UNC13A. *Nature* **603**, 124–130 (2022).
18. Sagner, A. & Briscoe, J. Establishing neuronal diversity in the spinal cord: a time and a place. *Development* **146**, dev182154 (2019).
19. Lupo, G., Harris, W. A. & Lewis, K. E. Mechanisms of ventral patterning in the vertebrate nervous system. *Nat. Rev. Neurosci.* **7**, 103–114 (2006).
20. Amoroso, M. W. et al. Accelerated high-yield generation of limb-innervating motor neurons from human stem cells. *J. Neurosci.* **33**, 574–586 (2013).
21. Du, Z.-W. et al. Generation and expansion of highly pure motor neuron progenitors from human pluripotent stem cells. *Nat. Commun.* **6**, 6626 (2015).
22. Rizzo, F. et al. Key role of SMN/SYNERP and RNA-Motif 7 in spinal muscular atrophy: RNA-Seq and motif analysis of human motor neurons. *Brain* **142**, 276–294 (2019).
23. Zhang, Q. et al. Single-cell analysis reveals dynamic changes of neural cells in developing human spinal cord. *EMBO Rep.* **22**, e52728 (2021).
24. Rayon, T., Maizels, R. J., Barrington, C. & Briscoe, J. Single-cell transcriptome profiling of the human developing spinal cord reveals a conserved genetic programme with human-specific features. *Development* **148**, dev199711 (2021).
25. Dann, E., Henderson, N. C., Teichmann, S. A., Morgan, M. D. & Marioni, J. C. Differential abundance testing on single-cell data using k-nearest neighbor graphs. *Nat. Biotechnol.* **40**, 245–253 (2022).
26. Sagner, A. et al. A shared transcriptional code orchestrates temporal patterning of the central nervous system. *PLoS Biol.* **19**, e3001450 (2021).
27. Van de Sande, B. et al. A scalable SCENIC workflow for single-cell gene regulatory network analysis. *Nat. Protoc.* **15**, 2247–2276 (2020).
28. Meng, H. et al. Loss of Parkinson’s disease-associated protein CHCHD2 affects mitochondrial crista structure and destabilizes cytochrome c. *Nat. Commun.* **8**, 15500 (2017).
29. Kee, T. R. et al. Mitochondrial CHCHD2: disease-associated mutations, physiological functions, and current animal models. *Front. Aging Neurosci.* **13**, 660843 (2021).
30. Arumugam, S., Garcera, A., Soler, R. M. & Tabares, L. Smn-deficiency increases the intrinsic excitability of motoneurons. *Front. Cell Neurosci.* **11**, 269 (2017).
31. Quinlan, K. A. et al. Hyperexcitability precedes motoneuron loss in the Smn2B<sup>-/-</sup> mouse model of spinal muscular atrophy. *J. Neurophysiol.* **122**, 1297–1311 (2019).
32. Brunet, A., Stuart-Lopez, G., Burg, T., Scekcic-Zahirovic, J. & Rouaux, C. Cortical circuit dysfunction as a potential driver of amyotrophic lateral sclerosis. *Front. Neurosci.* **14**, 363 (2020).
33. Sibilla, S. & Ballerini, L. GABAergic and glycinergic interneuron expression during spinal cord development: dynamic interplay between inhibition and excitation in the control of ventral network outputs. *Prog. Neurobiol.* **89**, 46–60 (2009).
34. Ramirez, A. et al. Investigation of new morpholino oligomers to increase survival motor neuron protein levels in spinal muscular atrophy. *Int. J. Mol. Sci.* **19**, 167 (2018).
35. Moulton, H. M. & Moulton, J. D. Morpholinos and their peptide conjugates: therapeutic promise and challenge for Duchenne muscular dystrophy. *Biochim. Biophys. Acta* **1798**, 2296–2303 (2010).
36. Bersani, M. et al. Cell-penetrating peptide-conjugated Morpholino rescues SMA in a symptomatic preclinical model. *Mol. Ther.* **30**, 1288–1299 (2022).
37. Gubitza, A. K., Feng, W. & Dreyfuss, G. The SMN complex. *Exp. Cell Res.* **296**, 51–56 (2004).
38. Yoo, H. et al. ATP-dependent chromatin remodeler CHD9 controls the proliferation of embryonic stem cells in a cell culture condition-dependent manner. *Biology* **9**, 428 (2020).
39. Guo, W. et al. HDAC6 inhibition reverses axonal transport defects in motor neurons derived from FUS-ALS patients. *Nat. Commun.* **8**, 861 (2017).
40. Chen, S. et al. Histone deacetylase 6 delays motor neuron degeneration by ameliorating the autophagic flux defect in a transgenic mouse model of amyotrophic lateral sclerosis. *Neurosci. Bull.* **31**, 459–468 (2015).
41. Mancinelli, S. & Lodato, S. Decoding neuronal diversity in the developing cerebral cortex: from single cells to functional networks. *Curr. Opin. Neurobiol.* **53**, 146–155 (2018).
42. Velasco, S., Paulsen, B. & Arlotta, P. 3D brain organoids: studying brain development and disease outside the embryo. *Annu. Rev. Neurosci.* **43**, 375–389 (2020).
43. Tambalo, M. & Lodato, S. Brain organoids: human 3D models to investigate neuronal circuits assembly, function and dysfunction. *Brain Res.* **1746**, 147028 (2020).
44. Paulsen, B. et al. Autism genes converge on asynchronous development of shared neuron classes. *Nature* **602**, 268–273 (2022).
45. Antón-Bolaños, N. et al. Brain chimeroids reveal individual susceptibility to neurotoxic triggers. *Nature* **631**, 142–149 (2024).
46. Mancinelli, S., Bariselli, S. & Lodato, S. The emergence of electrical activity in human brain organoids. *Stem Cell Rep.* **20**, 102632 (2025).
47. Ogura, T., Sakaguchi, H., Miyamoto, S. & Takahashi, J. Three-dimensional induction of dorsal, intermediate and ventral spinal cord tissues from human pluripotent stem cells. *Development* **145**, dev162214 (2018).
48. Faustino Martins, J.-M. et al. Self-organizing 3D human trunk neuromuscular organoids. *Cell Stem Cell* **26**, 172–186.e6 (2020).
49. Grass, T. et al. Isogenic patient-derived organoids reveal early neurodevelopmental defects in spinal muscular atrophy initiation. *Cell Rep. Med* **5**, 101659 (2024).
50. Galimberti, M. et al. Huntington’s disease cellular phenotypes are rescued non-cell autonomously by healthy cells in mosaic telecephalic organoids. *Nat. Commun.* **15**, 6534 (2024).

51. Barnat, M. et al. Huntington's disease alters human neurodevelopment. *Science* **369**, 787–793 (2020).
52. Galgoczi, S. et al. Huntingtin CAG expansion impairs germ layer patterning in synthetic human 2D gastruloids through polarity defects. *Development* **148**, dev199513 (2021).
53. Faravelli, I. & Corti, S. Spinal muscular atrophy - challenges in the therapeutic era. *Nat. Rev. Neurol.* **16**, 655–656 (2020).
54. Motyl, A. A. L. et al. Pre-natal manifestation of systemic developmental abnormalities in spinal muscular atrophy. *Hum. Mol. Genet.* **29**, 2674–2683 (2020).
55. Tharanetharan, A. et al. Functional abnormalities of cerebellum and motor cortex in spinal muscular atrophy mice. *Neuroscience* **452**, 78–97 (2021).
56. Simon, C. M. et al. A stem cell model of the motor circuit uncouples motor neuron death from hyperexcitability induced by SMN deficiency. *Cell Rep.* **16**, 1416–1430 (2016).
57. Wainger, B. J. et al. Intrinsic membrane hyperexcitability of amyotrophic lateral sclerosis patient-derived motor neurons. *Cell Rep.* **7**, 1–11 (2014).
58. Burg, T. et al. Absence of subcerebral projection neurons is beneficial in a mouse model of amyotrophic lateral sclerosis. *Ann. Neurol.* **88**, 688–702 (2020).
59. Marques, C., Burg, T., Scekcic-Zahirovic, J., Fischer, M. & Rouaux, C. Upper and lower motor neuron degenerations are somatotopically related and temporally ordered in the Sod1 mouse model of amyotrophic lateral sclerosis. *Brain Sci.* **11**, 369 (2021).
60. Finkel, R. S. et al. Nusinersen versus sham control in infantile-onset spinal muscular atrophy. *N. Engl. J. Med.* **377**, 1723–1732 (2017).
61. Duan, D., Goemans, N., Takeda, S., Mercuri, E. & Aartsma-Rus, A. Duchenne muscular dystrophy. *Nat. Rev. Dis. Prim.* **7**, 1–19 (2021).
62. Corti, S. et al. Genetic correction of human induced pluripotent stem cells from patients with spinal muscular atrophy. *Sci. Transl. Med.* **4**, 165ra162 (2012).
63. Hensel, N. et al. Impairment of the neurotrophic signaling hub B-Raf contributes to motoneuron degeneration in spinal muscular atrophy. *Proc. Natl. Acad. Sci. USA* **118**, e2007785118 (2021).
64. Taiana, M. et al. Molecular analysis of SMARD1 patient-derived cells demonstrates that nonsense-mediated mRNA decay is impaired. *J. Neurol. Neurosurg. Psychiatry* **93**, 908–910 (2022).
65. Ronchi, D. et al. Novel splice-site mutation in SMN1 associated with a very severe SMA-I phenotype. *J. Mol. Neurosci.* **56**, 212–215 (2015).
66. Pagliari, E. et al. Targeting STMN2 for neuroprotection and neuromuscular recovery in Spinal Muscular Atrophy: evidence from in vitro and in vivo SMA models. *Cell. Mol. Life Sci.* **82**, 29 (2024).
67. Carpenter, A. E. et al. CellProfiler: image analysis software for identifying and quantifying cell phenotypes. *Genome Biol.* **7**, R100 (2006).
68. Schindelin, J. et al. Fiji: an open-source platform for biological-image analysis. *Nat. Methods* **9**, 676–682 (2012).
69. Monteverdi, A., Di Domenico, D., D'Angelo, E. & Mapelli, L. Anisotropy and frequency dependence of signal propagation in the cerebellar circuit revealed by high-density multielectrode array recordings. *Biomedicines* **11**, 1475 (2023).
70. Wolf, F. A., Angerer, P. & Theis, F. J. SCANPY: large-scale single-cell gene expression data analysis. *Genome Biol.* **19**, 15 (2018).
71. Wolock, S. L., Lopez, R. & Klein, A. M. Scrublet: computational identification of cell doublets in single-cell transcriptomic data. *Cell Syst.* **8**, 281–291.e9 (2019).
72. Gayoso, A. et al. A Python library for probabilistic analysis of single-cell omics data. *Nat. Biotechnol.* **40**, 163–166 (2022).
73. Traag, V. A., Waltman, L. & van Eck, N. J. From Louvain to Leiden: guaranteeing well-connected communities. *Sci. Rep.* **9**, 5233 (2019).
74. Ahlmann-Eltze, C. & Huber, W. Comparison of transformations for single-cell RNA-seq data. *Nat. Methods* **20**, 665–672 (2023).
75. Muzellec, B., Teleńczuk, M., Cabeli, V. & Andreux, M. PyDESeq2: a Python package for bulk RNA-seq differential expression analysis. *Bioinformatics* **39**, btad547 (2023).
76. Badia-i-Mompel, P. et al. decoupleR: ensemble of computational methods to infer biological activities from omics data. *Bioinform. Adv.* **2**, vbac016 (2022).
77. Lange, M. et al. CellRank for directed single-cell fate mapping. *Nat. Methods* **19**, 159–170 (2022).
78. Gulati, G. S. et al. Single-cell transcriptional diversity is a hallmark of developmental potential. *Science* **367**, 405–411 (2020).
79. Moerman, T. et al. GRNBoost2 and Arboreto: efficient and scalable inference of gene regulatory networks. *Bioinformatics* **35**, 2159–2161 (2019).
80. AUCell. *Bioconductor* <http://bioconductor.org/packages/AUCell/>.
81. Setty, M. et al. Characterization of cell fate probabilities in single-cell data with Palantir. *Nat. Biotechnol.* **37**, 451–460 (2019).
82. Faure, A. J. et al. Mapping the energetic and allosteric landscapes of protein binding domains. *Nature* **604**, 175–183 (2022).
83. Petitpré, C. et al. Single-cell RNA-sequencing analysis of the developing mouse inner ear identifies molecular logic of auditory neuron diversification. *Nat. Commun.* **13**, 3878 (2022).
84. DeTomaso, D. & Yosef, N. Hotspot identifies informative gene modules across modalities of single-cell genomics. *Cell Syst.* **12**, 446–456.e9 (2021).
85. De Donno, C. et al. Population-level integration of single-cell datasets enables multi-scale analysis across samples. *Nat. Methods* **20**, 1683–1692 (2023).
86. Lotfollahi, M. et al. Mapping single-cell data to reference atlases by transfer learning. *Nat. Biotechnol.* **40**, 121–130 (2022).
87. He, Z. et al. An integrated transcriptomic cell atlas of human neural organoids. *Nature* **635**, 690–698 (2024).
88. Dobin, A. et al. STAR: ultrafast universal RNA-seq aligner. *Bioinformatics* **29**, 15–21 (2013).
89. Shen, S. et al. rMATS: robust and flexible detection of differential alternative splicing from replicate RNA-Seq data. *Proc. Natl. Acad. Sci. USA* **111**, E5593–E5601 (2014).
90. Zhou, Y. et al. Metascape provides a biologist-oriented resource for the analysis of systems-level datasets. *Nat. Commun.* **10**, 1523 (2019).

## Acknowledgements

The authors thank Associazione Centro Dino Ferrari for support, and the Humanitas Genomic Unit (HUGE) and Humanitas Bioinformatic Unit for technical support in single-cell sequencing experiments and analysis. We acknowledge Teresa Rayon (Babraham Institute, Cambridge, UK) for sharing counts of human fetal pMN and MN cell populations and Hynek Wichterle for sharing HB9 antibody (Motor Neuron Center, Columbia University, New York, NY). We acknowledge Dario Ronchi for precious comments and Stefania Sempregoni for technical support. We acknowledge Prof. Hong Moulton for morpholino-peptide conjugation. We would also like to acknowledge the following sources of funding. Italian Ministry of Health grant RF-2018-12366357 (S.C.), Italian Ministry of Health RF-2016-02362317 (G.C.), Italian Ministry of Health Fondazione IRCCS Ca' Granda Ospedale Maggiore Policlinico, Ricerca Corrente 230 2026 (G.C. and S.C.), Italian Ministry of Health PNRR-POC-2023-12377653 (S.C.). Telethon Foundation GGP14025 (M.N.), Italian Ministry of Health 5 × 1000 Ricerca Sanitaria-Italian Ministry of Health (S.L.), Italian Ministry of Health RF2018-12365280 (S.L.), Cariplo Giovani 2019-1785 (S.L.), Fondazione Umberto Veronesi (M.T.), and ERC Starting grant IMPACT 101043003 (S.L.), Ricerca Finalizzata GR-2019-12368561 (S.L.). Work supported by #NEXTGENERATIONEU (NGEU) and funded by the Ministry of University and Research (MUR), National Recovery and Resilience Plan (NRRP), project MNESYS (PE0000006)—A Multiscale

integrated approach to the study of the nervous system in health and disease (DN. 1553 11.10.2022) to E.P. and E.D. The Department of Pathophysiology and Transplantation, University of Milan, is funded by the Italian Ministry of Education and Research (MUR): Dipartimenti di Eccellenza Program 2023 to 2027.

## Author contributions

S.C., M.N., S.L., I.F., M.T., and P.R. conceived and designed the research project. M.N., P.R., M.R., G.F., A.D.A., and L.C. performed experiments and collected data regarding iPSCs generation and characterization. P.R., I.F., and A.D.A. generated and characterized spinal cord organoids. F.B. helped generating and characterizing spinal cord organoids. M.T., P.R., and I.F. generated and characterized brain organoids. S.M. and M.T. performed image acquisition and S.M., M.T., and P.R. performed image quantification. L.M. and E.D. conducted MEA recording and analyses with the help of E.P., and C.C. imaged and quantified TUNEL analyses together with P.R. I.F. and P.R. performed statistical analyses on aggregated data for SOX2 and TUJ1 counts. C.P., S.M., and M.T. performed single-cell RNA-seq experiments and P.K. and I.S. performed the relative computational analyses. M.M. and E.M.P. analyzed bulk RNA-seq and splicing data. G.C. and S.P. contributed to data discussion and supervision of I.F. and P.R. I.F., P.R., M.T., S.L., and S.C. wrote the manuscript with the critical contribution of all the authors. S.L. and S.C. contributed equally to this work. All authors critically reviewed and approved the final version of the manuscript.

## Competing interests

The authors declare no competing interests.

## Additional information

**Supplementary information** The online version contains supplementary material available at <https://doi.org/10.1038/s41467-025-67725-1>.

**Correspondence** and requests for materials should be addressed to Simona Lodato or Stefania Corti.

**Peer review information** *Nature Communications* thanks Yoshiho Ikeuchi and the other, anonymous, reviewers for their contribution to the peer review of this work. A peer review file is available.

**Reprints and permissions information** is available at <http://www.nature.com/reprints>

**Publisher's note** Springer Nature remains neutral with regard to jurisdictional claims in published maps and institutional affiliations.

**Open Access** This article is licensed under a Creative Commons Attribution-NonCommercial-NoDerivatives 4.0 International License, which permits any non-commercial use, sharing, distribution and reproduction in any medium or format, as long as you give appropriate credit to the original author(s) and the source, provide a link to the Creative Commons licence, and indicate if you modified the licensed material. You do not have permission under this licence to share adapted material derived from this article or parts of it. The images or other third party material in this article are included in the article's Creative Commons licence, unless indicated otherwise in a credit line to the material. If material is not included in the article's Creative Commons licence and your intended use is not permitted by statutory regulation or exceeds the permitted use, you will need to obtain permission directly from the copyright holder. To view a copy of this licence, visit <http://creativecommons.org/licenses/by-nc-nd/4.0/>.

© The Author(s) 2025

<sup>1</sup>Dino Ferrari Centre, Neuroscience Section, Department of Pathophysiology and Transplantation (DEPT), University of Milan, Milan, Italy. <sup>2</sup>Department of Biomedical Sciences, Humanitas University, Pieve Emanuele, MI, Italy. <sup>3</sup>Department of Brain and Behavioral Sciences, University of Pavia, Pavia, Italy. <sup>4</sup>IRCCS Humanitas Clinical and Research Hospital, Rozzano-Milan, Italy. <sup>5</sup>Department of Neurosciences, Foundation IRCCS Ca' Granda Ospedale Maggiore Policlinico, SC Neurology, Milan, Italy. <sup>6</sup>Istituto Nazionale di Genetica Molecolare "Romeo ed Enrica Invernizzi", Milan, Italy. <sup>7</sup>Institute of Genetic and Biomedical Research, UoS of Milan, National Research Council, Rozzano, MI, Italy. <sup>8</sup>Bioinformatics Unit, IRCCS Humanitas Clinical and Research Hospital, Rozzano-Milan, Italy. <sup>9</sup>Digital Neuroscience Center, IRCCS Mondino Foundation, Pavia, Italy. <sup>10</sup>Center for Motor Neuron Biology and Disease, Columbia University, New York, NY, USA. <sup>11</sup>Department of Pathology and Cell Biology, Columbia University, New York, NY, USA. <sup>12</sup>Department of Neurology, Columbia University, New York, NY, USA. <sup>13</sup>Department of Neuroscience, Columbia University, New York, NY, USA. <sup>14</sup>Foundation IRCCS Ca' Granda Ospedale Maggiore Policlinico, SSD Neuromuscular and rare diseases, Milan, Italy. <sup>15</sup>Present address: Department of Stem Cell and Regenerative Biology, Harvard University, Cambridge, MA, USA. <sup>16</sup>Present address: Department of Systems Biology, Columbia University, New York, NY, USA. <sup>17</sup>Present address: Human Technopole, Milan, Italy. <sup>18</sup>These authors contributed equally: Irene Faravelli, Paola Rinchetti, Monica Tambalo. ✉ e-mail: [simona.lodato@hunimed.eu](mailto:simona.lodato@hunimed.eu); [stefania.corti@unimi.it](mailto:stefania.corti@unimi.it)